JGR Space Physics

RESEARCH ARTICLE
10.1029/2024JA033456

Statistical Analysis of Ultra-Low-Frequency Total Electron Content Disturbances: Relationship to Magnetospheric Waves

Michael D. Hartinger[1,2], Xueling Shi[3,4], Olga Verkhoglyadova[5], Xing Meng[6], Dogacan Su Ozturk[7], Angelyn Moore[5], Yangyang Shen[2], Anton Artemyev[2], D. Megan Gillies[8], and Vassilis Angelopoulos[2]

[1]Space Science Institute, Boulder, CO, USA, [2]Department of Earth, Planetary and Space Sciences, University of California Los Angeles, Los Angeles, CA, USA, [3]Department of Electrical and Computer Engineering, Virginia Tech, Blacksburg, VA, USA, [4]High Altitude Observatory, National Center for Atmospheric Research, Boulder, CO, USA, [5]Jet Propulsion Laboratory, California Institute of Technology, Pasadena, CA, USA, [6]School of Earth and Space Sciences, University of Science and Technology of China, Hefei, China, [7]Geophysical Institute, University of Alaska, Fairbanks, Fairbanks, AK, USA, [8]Mount Royal University, Calgary, AB, Canada

Key Points:

- Magnetospheric Ultra Low Frequency (ULF) waves drive auroral zone Total Electron Content (TEC) variations (2–50 mHz)
- TEC variation amplitude correlates with ground magnetic variation amplitude, and the correlation depends on magnetic field component
- TEC variation amplitude correlates with Kp, AE, and solar wind speed, and the largest amplitudes usually occur near local midnight

Supporting Information:

Supporting Information may be found in the online version of this article.

Correspondence to:

M. D. Hartinger,
mhartinger@spacescience.org

Citation:

Hartinger, M. D., Shi, X., Verkhoglyadova, O., Meng, X., Ozturk, D. Su., Moore, A., et al. (2025). Statistical analysis of ultra-low-frequency total electron content disturbances: Relationship to magnetospheric waves. *Journal of Geophysical Research: Space Physics*, *130*, e2024JA033456. https://doi.org/10.1029/2024JA033456

Received 19 OCT 2024
Accepted 2 APR 2025

Abstract Disturbances in ionospheric Total Electron Content (dTEC) with frequencies of ∼1–100 mHz can be driven from above by processes in the magnetosphere and below by processes on the Earth's surface and lower atmosphere. Past studies showed the potential of dTEC as a diagnostic of magnetospheric Ultra Low Frequency (ULF) wave activity and demonstrated that ULF dTEC can impact space weather by, for example, changing ionospheric conductance. However, most past work has focused on single event studies, lacked magnetospheric context, or used sampling rates too low to capture most ULF waves. Here, we perform a statistical study using Time History of Events and Macrsoscale Interactions during Substorms (THEMIS) satellite conjunctions with a ground-based magnetometer and Global Navigation Satellite System (GNSS) receiver at ∼65° magnetic latitude. We find that magnetospheric ULF waves generate dTEC variations across the broad range of frequencies examined in this study (∼2–50 mHz), and that ULF dTEC wave power is correlated with Kp, AE, solar wind speed, and magnetic field wave power observed in the magnetosphere and on the ground. We further find that magnetospheric ULF waves generate dTEC amplitudes up to $< \sim 4$ TECU (∼30% background), with the largest amplitudes occurring during geomagnetically active conditions, at frequencies below 7 mHz, and at local times near midnight. We finally discuss the implications of our results for magnetosphere-ionosphere coupling and remote sensing techniques related to ULF waves.

Plain Language Summary The Earth's upper atmosphere includes a region of charged particles (ions and electrons) known as the ionosphere. The ionosphere is dynamic, with variations on a range of timescales and spatial scales including electron density variations with frequencies of ∼1–100 mHz. These variations have been linked to (a) waves in the neutral atmosphere related to terrestrial weather and disturbances such as earthquakes and volcanoes and (b) disturbances in near-Earth space. Many studies have successfully used "Total Electron Content" (TEC), a quantity corresponding to the number of electrons on a line of sight between a ground-based receiver and satellite, to study ionospheric electron variations, but it is challenging to use TEC to understand the sources of variations in the ∼1–100 mHz range due to difficulties discriminating between driving mechanisms below and above the ionosphere. We address this challenge by using a combination of satellite measurements and ground-based measurements, finding that ∼2–50 mHz TEC variations are often associated with plasma waves in near-Earth space, suggesting that TEC can be more widely used to remote sense plasma waves. We further find TEC variation amplitudes can be large enough to cause space weather impacts, though more work is needed to quantify these impacts.

1. Introduction

1.1. Total Electron Content Perturbations and Space Weather Impacts

The total electron content (TEC) or slant TEC (STEC, measured in TECU, 1 TECU = 10^{16} electrons/m^2) is the integrated electron number density along a link between a transmitting satellite of the Global Navigation Satellite System (GNSS) constellation and a ground-based GNSS station. TEC is estimated from the phase difference

between the two carrier frequencies (Hajj & Romans, 1998; Vorob'Ev & Krasil'nikova, 1994) and is used for ionospheric remote sensing, monitoring, and investigation. Vertical TEC (VTEC) is the vertically integrated electron number density. It can be obtained from the STEC by a mapping technique that applies an elevation angle dependent factor to STEC to obtain VTEC, with the scaling factor calculated by assuming a simplified electron density altitude dependence (e.g., Section 3.1 and Figure 3 in Mannucci et al. (1998), note the scaling factor is between roughly 1 and 1.5 for elevation angles considered in this study). Hereafter, we use TEC to denote vertical TEC. TEC perturbations can be extracted from GNSS-derived TEC timeseries by removing the background trend in the TEC timeseries and band-pass filtering (e.g., Komjathy et al., 2016). For the purposes of this study, a TEC perturbation (dTEC) is defined as a change in TEC with a frequency of the order ∼1–100 mHz (the lower end of the Ultra Low Frequency [ULF] range described in Section 1.2).

Disturbances in ionospheric electron density represented by ULF dTEC can be driven from altitudes below, inside, and above the ionosphere by several processes. dTEC in the ∼1–10 mHz range can be caused by lower atmospheric forcing of the ionosphere with acoustic-gravity waves from processes such as earthquakes, volcanic eruptions, and explosions (see reviews by Meng et al., 2019; Huang et al., 2019). Many dTEC events caused by lower atmospheric forcing are related to Traveling Ionospheric Disturbances (TID), which can sub-categorized according to their properties (Huang et al., 2019, and references therein):

1. Large-scale TID (LSTID) have horizontal wavelengths in the ionosphere >1,000 km, typical horizontal velocities of 400–1,000 m/s, and typical frequencies of ∼0.093–0.56 mHz.
2. Medium-scale TID (MSTID) have wavelengths ∼400–1,000 km, velocities ∼100–300 m/s, and typical frequencies of ∼0.28–1.4 mHz.
3. Small-scale TID (SSTID) have wavelengths ∼10–100 km, velocities <200 m/s, and wave frequencies of a few mHz. They are heavily damped when propagating to higher altitudes (>∼200 km), thus associated dTEC with large amplitudes are less likely to occur in the F-region ionosphere when driven from lower atmosphere forcing (Vadas, 2007).

TIDs can have a range of dTEC amplitudes that vary according to the specific driving mechanism, distance from the source region, etc. For example, earthquake-related TID often have dTEC amplitudes ∼0.2–0.5 TECU near the source region, with the most extreme cases (largest magnitude earthquakes) having amplitudes ∼5 TECU (Heki, 2021).

dTEC perturbations in the ULF range can also be driven by processes occurring in the magnetosphere and ionosphere. For example, transient, impulsive disturbances in the solar wind lead to transient field-aligned currents that couple to TEC perturbations (Jayachandran et al., 2011; Pilipenko et al., 2018; Pradipta et al., 2014), dayside reconnection has been linked to dTEC in the polar cap (Watson et al., 2016b), and substorm-related precipitation has also been linked to dTEC (Watson et al., 2011). Polar cap patches and other structures on a range of spatial scales in the ionosphere can also be convected past receivers and observed as dTEC (Watson et al., 2016a). Finally, magnetospheric ULF wave activity has also frequently been linked to periodic dTEC (e.g., Belakhovsky et al., 2016; Kozyreva et al., 2020), as described in the next section. Past studies have noted the difficulties in discriminating dTEC/TIDs driven from above (magnetosphere/ionosphere) and below (atmosphere) due to similar temporal scales, spatial scales, and speeds. For example, Dinsmore et al. (2021) noted that a globally coherent dTEC structure likely related to auroral forcing from above could "masquerade as an MSTID" when viewed locally with a limited set of observations.

1.2. Magnetospheric ULF Waves and Their Link to TEC Perturbations

Jacobs et al. (1964) defines the ULF range for magnetospheric plasma waves, also referred to as pulsations, as being ∼1–5,000 mHz. ULF waves are further sub-categorized by Jacobs et al. (1964) according to smaller frequency bands and whether they last many wave cycles ("Pc" or "pulsations continuous") or only a few cycles ("Pi" or "pulsations irregular"). In this study, we only consider the lower part of the ULF band, including the Pc5 (2–7 mHz), Pc4 (7–22 mHz), Pi2 (7–22 mHz), and part of the Pc3 range (22–100 mHz). ULF waves at these frequencies can carry significant energy to the ionosphere and play important roles in magnetosphere-ionosphere coupling. For example, Buchert et al. (1999), Pilipenko, Belakhovsky, Kozlovsky, et al. (2014), and Wang et al. (2020) used Incoherent Scatter Radar (ISR) measurements to show that ULF waves with frequencies from ∼1–10 mHz can significantly modulate the ionospheric electron density at a range of altitudes and affect Pedersen, Hall, and Alfvén conductances, in some cases by a factor of ∼8. These and other studies discussed how

these large modulations in electron density and conductivity affect M-I coupling processes and space weather, including (a) the geomagnetic response (Buchert et al., 1999; Pilipenko, Belakhovsky, Kozlovsky, et al., 2014) and related Geomagnetically Induced Current (GIC) and (b) heating in the I-T system (e.g., Lotko & Zhang, 2018; Verkhoglyadova et al., 2018).

Electron density modulations linked to ULF waves can also be observed in TEC. These dTEC events have been observed in the polar cap (e.g., Watson et al., 2016a), auroral zone (e.g., Pilipenko, Belakhovsky, Murr, et al., 2014), mid-latitude (e.g., Davies & Hartmann, 1976), and low-latitude regions (e.g., Yizengaw et al., 2013, 2018). They occur at a range of geomagnetic activity levels (Okuzawa & Davies, 1981) with frequencies from ∼1–100 mHz (Skone, 2009; Watson, Jayachandran, Singer, et al., 2016; Watson et al., 2015). Case studies show that ULF wave dTEC events have amplitudes as large as 7 TECU while dTEC/TEC has ranged from 0.1% to 35% (Watson et al., 2015, see Table 1 in that study).

Poole and Sutcliffe (1987) proposed several mechanisms for magnetospheric ULF waves to drive dTEC, sorting them into categories according to different terms in the electron continuity equation. Pilipenko, Belakhovsky, Murr, et al. (2014) explored several possible mechanisms linking dTEC to ULF waves with a focus on higher latitudes, including for example, ULF wave-modulated precipitation of energetic electrons that can affect ionospheric conductivities (e.g., Buchert et al., 1999; Wang et al., 2020) and periodic plasma flow related to Alfvén wave field-aligned currents (Belakhovsky et al., 2016; Kozyreva et al., 2020; Pilipenko et al., 2018). Regardless of the mechanism(s) involved, many ULF wave modes exist in the Earth's magnetosphere that can potentially generate dTEC. For the purpose of this study, there are a few important wave modes to consider:

1. Toroidal mode: Usually detected in the azimuthal component of the magnetic field in the magnetosphere and the north-south component of the magnetic field on the ground; the latter is due to ionospheric modification of the signal that typically causes a 90° rotation above and below the ionosphere (Southwood & Hughes, 1983). In realistic geometries and for realistic assumptions about wave properties (e.g., finite wave packets rather than infinite sine waves), disturbances in the vertical component of the magnetic field may also be observed and can be related to localized wave source regions (Southwood & Hughes, 1983). The vertical component of the magnetic field on the ground has been associated with field-aligned current related to Alfvén waves, with some models predicting the intensity of the vertical disturbance on the ground will maximize near the location of maximum field-aligned current intensity above the ionosphere (Lanzerotti et al., 1990). Other studies predict vertical magnetic field disturbances on the ground may occur due to Hall currents under non-uniform ionospheric conductance conditions (Walker et al., 1979) or be related to induced currents in the ground (Juusola et al., 2020; Pulkkinen & Engels, 2005).
2. Poloidal mode: Usually detected in the radial component of the magnetic field in the magnetosphere and the east-west component of the magnetic field on the ground. Similar to the toroidal mode, a 90° rotation occurs (Southwood & Hughes, 1983) and vertical magnetic disturbances can be observed due to several different effects (see above). Unlike the toroidal mode, poloidal modes are sometimes associated with energy sources that lead to the generation of waves with small azimuthal wavelengths which tend to have minimal ground magnetic signals due to an ionospheric screening effect (Hughes, 1974), but this is not always the case.
3. Magnetosonic mode: Usually detected in the compressional component of the magnetic field in the magnetosphere, these waves should create a magnetic disturbance on the ground (Kivelson & Southwood, 1988; Sciffer & Waters, 2011). For low frequency waves, locations away from resonances, and locations in the auroral zone (i.e., background magnetic field roughly vertical), the magnetic signal is relatively unaffected by the ionosphere; thus disturbances in the same components of the magnetic field will be observed above and below the ionosphere (Kivelson & Southwood, 1988).

The tendency of wave-related disturbances to be observed in a particular component of the magnetic field is often used as a shorthand for wave polarization and as a diagnostic for identifying the ULF wave modes listed above (e.g., Takahashi et al., 2012). It is not a definitive test in events where more than one wave mode is present or mode conversion is occurring; in these cases, relative power in different wave magnetic or electric field components, ellipticity, multi-point observations, and other tests may be required to isolate particular wave modes (e.g., Hartinger et al., 2013). However, comparisons of wave power in different components of the magnetic field can at least be used as a starting point to identify which wave modes may be present or which occur most frequently in a statistical analysis.

1.3. Unresolved Questions and Motivation for Present Study

There are several motivations to better establish the connections between magnetospheric ULF waves and dTEC:

1. Advances in remote sensing techniques: Observations of global ULF wave properties are needed for a range of space weather models and applications (e.g., Hartinger et al., 2022; Ozeke et al., 2020). dTEC observations have been proposed as a remote sensing method for ULF waves (Watson, Jayachandran, Singer, et al., 2016; Watson et al., 2015; Zhai et al., 2021) that can address many sampling biases that affect satellite and other ground-based measurements while also filling gaps in spatial coverage, but it has thus far only been used in case studies. Routine use of dTEC observations for remote sensing ULF waves requires statistical studies comparing wave magnetic or electric field measurements with dTEC measurements, and this is a key motivation for this study.
2. Improved understanding of M-I coupling processes and space weather impacts: Past studies have found dTEC amplitudes related to magnetospheric ULF waves as large as 7 TECU while dTEC/TEC has ranged from 0.1% to 35% (Watson et al., 2015). These large modulations, particularly 35% of background levels, represent a challenge to typical M-I coupling models related to, for example, ULF waves that assume a static ionosphere as a boundary condition and/or linear perturbations of wave disturbances to background values of magnetic field, electron density, etc. (Allan et al., 1991; Lysak, 1990; Southwood & Hughes, 1983), with ground magnetometer observations already suggesting these models need modification (Pilipenko, Belakhovsky, Kozlovsky, et al., 2014). dTEC can also ultimately indicate the development of ionospheric irregularities and/or changes in height-integrated ionospheric conductance (e.g., Wang et al., 2020) which in turn can lead to a range of space weather impacts, including effects on geomagnetic perturbations (Buchert et al., 1999; Pilipenko, Belakhovsky, Kozlovsky, et al., 2014) related to GIC (e.g., Pulkkinen et al., 2017; Welling, 2019), effects on ionosphere-thermosphere heating rates (Smith et al., 2023; Verkhoglyadova et al., 2018), and effects on GNSS positioning (e.g., Béniguel et al., 2009; Waters & Cox, 2009). Identifying the conditions during which ULF dTEC occur and statistically quantifying their amplitude is thus another important motivation of this study.

The above discussion motivates several questions related to ULF dTEC needed to routinely use dTEC as a diagnostic for magnetospheric ULF wave activity and assess ULF dTEC space weather impacts: "Over what period ranges do magnetospheric ULF waves drive dTEC?," "Does magnetospheric ULF wave magnetic field amplitude correlate with ULF dTEC amplitude and, if so, could it be used as a magnetic field amplitude proxy?," "What factors control ULF dTEC occurrence rates and lead to the largest amplitudes?" Several challenges have prevented progress in addressing questions such as these: (a) most work has focused on single case events or a small number of case studies, making it difficult to determine whether significant dTEC are routinely driven by these waves; moreover, most past studies did not include magnetically conjugate satellite measurements, making it difficult to definitively link magnetospheric ULF waves to dTEC, (b) some past studies linking magnetospheric ULF waves to dTEC did not consider the possibility of driving from atmospheric waves related to surface disturbances, yet we know these disturbances couple to dTEC in the ULF range, (c) TEC measurements are commonly available at 30 s resolution, but $\sim$<5-s measurements are needed to investigate a large portion of the ULF band.

In this study, we address these challenges through use of $\sim$<3s measurements in a statistical analysis of dTEC at $\sim$65° magnetic latitude, supported by $\sim$7 years of satellite measurements as well as ground magnetometers. This novel analysis requires significant discussion of the several different data sets, data processing techniques to link and compare the data sets (field line tracing, signal processing, etc), and their related sampling biases. For this reason, we shall not attempt a comprehensive statistical analysis of all types of ULF waves across all conditions and at all latitudes. Instead, for brevity we focus on a few critical results in the auroral zone related to the questions in the previous paragraph, and we develop an analysis framework and database (Hartinger, 2024a, 2024b) that can be applied to follow-on studies targeting additional properties of ULF dTEC events. We also focus on monochromatic waves rather than perturbations with a broadband frequency spectrum that overlap the ULF band.

2. Methodology

2.1. Instrumentation and Data Sets

For satellite observations, we use measurements from the fluxgate magnetometer (Auster et al., 2008, FGM) and Electrostatic Analyzer (McFadden et al., 2008, ESA) instruments on NASA's five-satellite Time History of Events and Macroscale Interactions during Substorms (THEMIS) mission (Angelopoulos, 2008). FGM data sampled at ∼3 s intervals (satellite spin period) from 3 of 5 THEMIS satellites with typical apogees near 12 Earth radii are used to obtain wave power spectral densities; the other two satellites are less useful for this study as they entered lunar orbit in 2010. We also use electron energy flux measurements from ESA to obtain a proxy for the field-aligned electron population (electrons available to precipitate) used in Supporting Information S1. Level-2 THEMIS data were obtained and initial processing performed using the open-source Python-based Space Physics Environment Data Analysis Software (PySPEDAS) framework (Grimes et al., 2022).

We also use solar wind measurements (propagated to Earth's bow shock) and geomagnetic activity indices for (a) magnetic field models used for field-line tracing and (b) statistical analysis of dTEC. We access both from NASA's Space Physics Data Facility OMNIWeb interface database. For this study, we only require hourly averaged values, though minute-averaged values are also stored in our database for future studies.

For remote sensing ULF wave activity from the ground, we use magnetometer measurements from the United States Geological Survey (USGS) Geomagnetism Program College (CMO) site sampled at 1.0 Hz (Love & Finn, 2011). CMO is located at geographic coordinates of 64.87° north and 147.86° west, and it has a geomagnetic latitude of 65.46° north based on the 2015 IGRF model. CMO magnetic field measurements are in geomagnetic coordinates, where x is magnetic north, z is vertical (directed down into the ground), and y completes the right hand orthogonal set. Finally, we use measurements from the FAIR GNSS receiver to estimate TEC time series. The FAIR receiver is located near Fairbanks, Alaska (geographic coordinates 64.978 north and 147.499° west) and was selected because of proximity to the CMO magnetometer. We utilized high-rate 1-s RINEX data for this station obtained from the NASA Crustal Dynamics Data Information System (CDDIS) archive of space geodesy data (https://cddis.nasa.gov/archive/gnss/data/highrate/).

We also take into account possible ULF dTEC activity driven from ground/lower atmosphere forcing by collecting earthquake information from USGS (https://earthquake.usgs.gov/earthquakes/search/) to obtain an earthquake catalogue, which covers all earthquakes that occurred between year 2012 and year 2019, when the epicenter falls within the Alaska region and moment magnitude $M_W \geq 6.0$. We also refer to volcanic eruption events in Alaska during 2012–2019 documented in Alaska Volcano Observatory (https://avo.alaska.edu/explore/eruptions). We found that no earthquakes or eruptions occurred in close proximity (time or space) to FAIR for the events we examined. Thus, we can proceed with our analysis without the complication of, for example, near-field effects of severe lower atmosphere forcing that may cause both dTEC and magnetic fluctuations (Surkov et al., 2023).

In this study, we develop a database that can be used for follow-on studies examining the sources of dTEC for a range of magnetic latitudes and local times as well as the altitude at which the dTEC modulation occurs and impacts of the dTEC on ionospheric conductance and other parameters. Thus, the rationale for some of our choices for time intervals to examine, specific geographic locations, etc. extends beyond the database needs for this particular study of dTEC in the auroral zone. We choose an analysis interval from 1 October 2012 to 1 October 2019 because of the availability of both THEMIS and Van Allen Probes satellites; although only THEMIS conjunctions will be examined in this study, Van Allen Probes conjunctions would be used for a follow-on study focusing on mid-latitude dTEC. We further focus on the CMO magnetometer and FAIR receiver due their close proximity to the Poker Flat ISR which will be used in a follow-on study.

2.2. Data Processing

In this sub-section, we describe the data processing pipeline, associated data reduction, and potential associated sampling biases. In Table S1 in Supporting Information S1 shows how each data processing step affects the number of events analyzed.

2.2.1. Satellite Conjunctions and Magnetic Field Line Tracing

In the first data processing step, we define a set of magnetic conjunction events between THEMIS-A, THEMIS-D, and THEMIS-E satellites and CMO/FAIR using the Tsyganenko (1989) model (T89) combined with IGRF and the Geopack library provided as part of the SPEDAS software package (Angelopoulos et al., 2019). While there are many empirical magnetic field models that could be used, T89 was selected (a) for its overall simplicity (only parameterized by Kp index) and (b) based on sensitivity tests comparing T89 with other more recent models (T96, T01) that were performed on a very similar THEMIS statistical data set in a past study (Hartinger et al., 2015) that found T89 was mostly consistent with in situ magnetic field measurements made by the satellite.

We performed magnetic field-line tracing every 1-min for all three THEMIS satellites for the period from 1 October 2012 to 1 October 2019. A magnetic conjunction is defined as follows:

1. The satellite footpoint, or location at which the magnetic field line intersects the Earth's ionosphere, is within a region of ±1.5° magnetic latitude and ±5° magnetic longitude of the FAIR receiver
2. The magnetic field measured by the satellite validates the T89 model used for tracing. In this case, a test is applied requiring the angle between the two vectors to be less than 10°.
3. The conjunction must last at least 15 min (i.e., the footpoint must be in the box for 15 min).
4. Duplicate conjunctions from multiple satellites are removed when within 60 min of each other to avoid double counting the same event. The precedence for conjunctions is THEMIS-E, THEMIS-D, and THEMIS-A. If a conjunction has already been identified by the THEMIS-E satellite within 60 min of a conjunction with THEMIS-D and THEMIS-A, the latter are discarded.

If there were gaps in the THEMIS position or magnetic field time series, or if the magnetic field data have contamination, no conjunction is identified.

The first four rows of Table S1 in Supporting Information S1 show how many events are identified when applying different criteria to the conjunctions. Our rationale for selecting the thresholds in the above list was based in part on our understanding of typical spatial scales (a spread of ±1.5° magnetic latitude roughly corresponds to <2 Earth radii, a moderate wavelength in the auroral zone) and event duration (15 min corresponds to a typical wave event duration for waves in the middle of our chosen frequency range) for ULF waves in the auroral zone. There is no ideal set of event time thresholds, conjunction box sizes, etc. that can fit all conditions and wave properties, and we acknowledge these choices can all lead to potential sampling biases. We discuss these biases further throughout the manuscript and address them by, for example, by cross-checking results between CMO/FAIR independently from THEMIS.

2.2.2. GNSS STEC and VTEC Data Processing

We created a data processing pipeline based on 1-s RINEX data obtained from the Crustal Dynamics Data Information System (CDDIS) high-rate archive. The GipsyX and Global Ionospheric Mapping (GIM) software developed at Jet Propulsion Laboratory was utilized to derive STEC and VTEC for the ULF wave event intervals (Bertiger et al., 2020; Komjathy et al., 2005; Martire et al., 2024). GipsyX is a versatile software package for GNSS data analysis for many applications. The STEC is converted to VTEC at an ionospheric pierce point (IPP) height of 450 km by using the standard mapping function (e.g., Mannucci et al., 1998). 450 km is an intermediate value chosen to reflect a typical median height for electron density (Mannucci et al., 1998), and it is widely used in analysis of ionospheric TEC, for example, in the generation of global TEC maps (Rideout & Coster, 2006). The choice of IPP altitude has little impact on the mapping function for the larger elevation angles we ultimately consider in this study. Measurements with elevation angles less than 10° were rejected in the initial processing, while later processing used a final cutoff of 30° (see below) with most events having elevation angles $>\sim 45°$ (Section 2.2.4 and Figure S1 in Supporting Information S1). We used GipsyX data handling utilities to prepare the input data by combining the 15-min high-rate RINEX files into lengthier observation sessions. The output TEC files for each ground station contain time stamps, multiple satellite-receiver pairs, elevation angles, locations of IPPs in geographic coordinates and VTEC in TECU. We only use VTEC for the statistical analysis, but we compared STEC and VTEC time series and found the properties of dTEC variations (amplitude, phase) were very similar.

As an additional data reduction step, we omitted multi-day events because arcs that span across UT midnight are subject to day-boundary discontinuities, due to the 24-hr length of the daily GNSS input data files. This

introduced a small sampling bias with less local time coverage in the post-noon sector (UT midnight), but it was not significant and did not affect our main conclusions as will be shown in a later figure; we do not stress fine scale local time variation trends in this study, only large scales over many hours (e.g., dusk vs. dawn).

2.2.3. Signal Processing and Database Construction

Step 1: Data Pre-Processing for Time Series and Power Spectra

The processing of time series and power spectra from satellite, ground magnetometer and TEC data involves several steps needed to ensure accuracy and consistency. First, a three-point smooth is applied to the 1-s VTEC and 1-s ground magnetometer time series, smoothing the data over a 3-s interval to be comparable with satellite data temporal resolution. Next, a common time array is created, consisting of evenly spaced 3-s samples for 1,024 points. This array spans from 512 points before to 512 points after the center of conjunction, covering a total of 51.2 min. The satellite, ground magnetometer, and VTEC measurements are then interpolated to match this common time array. Following this, the magnetic field (B) from satellite and ground magnetometer and VTEC time series corresponding to these 1,024 points centered on the conjunction are extracted. A polynomial fit is applied to the B time series, and the resulting polynomial is subtracted to obtain the perturbations (dBsat and dBground); dBsat is initially in Geocentric Solar Magnetospheric (GSM) coordinates (to be transformed, see below) while dBground is in a standard magnetic coordinate system for ground magnetometers where x is towards magnetic north, z is directed down into the Earth, and y completes the right-hand orthogonal set (roughly eastward). The same detrending process is applied to the TEC time series to get dTEC. To more easily associate dBsat with different wave modes, a coordinate transformation is applied. The mean B in the conjunction window is calculated. Using this mean B, the satellite dBsat is rotated into field-aligned coordinates (FAC) where z is parallel to the mean B, y is in the local azimuthal direction for GSM cylindrical coordinates, and x completes the right-hand orthogonal set and is directed radially outward; these FAC coordinates can be more directly associated with specific ULF wave modes (Section 1.2). A Discrete Fourier Transform (DFT) is then performed on all detrended time series to obtain the power spectrum. Finally, the power spectral density, along with the frequency array, is stored in a HDF5 file for each conjunction event. This approach ensures consistent processing and analysis of the power spectra data across different data sets. The same processing is applied to each conjunction event. An example THEMIS conjunction event is shown in Figure 1, with the location of the IPP at 450 km for different GPS satellites in Figure 1a, detrended time series shown in Figure 1b (panels 3–5 from the top) and an example dTEC power spectra in Figure 1c (black curve). Note that we only show the IPP plot in Figure 1c for broad context since we don't know the altitude of the peak ULF dTEC modulation in this event thus don't know what reference altitude to pick for the plot.

Step 2: Post-Processing for Wave Power Peaks: Frequency Domain Analysis

The post-processing of the data for frequency domain analysis involves several steps to identify and analyze significant peaks in the power spectra; these steps are based on analysis techniques that have been employed successfully in other studies seeking to identify and statistically examine ULF wave events in satellite and ground-based measurements (e.g., Cao et al., 1994; Hartinger et al., 2013; Takahashi et al., 2012). First, the power spectra are obtained from the HDF5 files constructed in Step 1. To reduce noise, a three-point smooth is applied to the wave power samples in the frequency domain, which maintains the frequency resolution (with bins approximately 0.3 mHz both before and after smoothing) but reduces the ability to discern small variations in frequency narrower than 0.9 mHz. Next, new variables are created for the smoothed power and frequency, focusing only on frequencies within the range of 0.65–50 mHz. A least-squares fit is performed on the logarithm of the smoothed power versus the logarithm of the frequency within the specified range. The value of this fit is subtracted from the original data, resulting in the log of the power ratio, which effectively normalizes the power spectrum (i.e., the power values are relative to background levels rather than absolute). The red line in Figure 1c is the least-square fit on the log scale, and the solid blue line is the subtracted PSD in log scale (i.e., the log of the power ratio). Significant peaks in the normalized power spectrum are identified using a peak-finding algorithm (Virtanen et al., 2020). The peak prominence was adjusted experimentally to find the ideal values for identifying significant peaks (using visual inspection, see Step 3 below), and a fixed prominence of 1 was finally chosen. Finally, the frequency and other properties of each significant peak are stored in one HDF5 file that is publicly available (Hartinger, 2024b). This file includes details such as the component or instrument where the peak was identified, the peak power spectral density before detrending, prominence, and peak width at half maximum. This

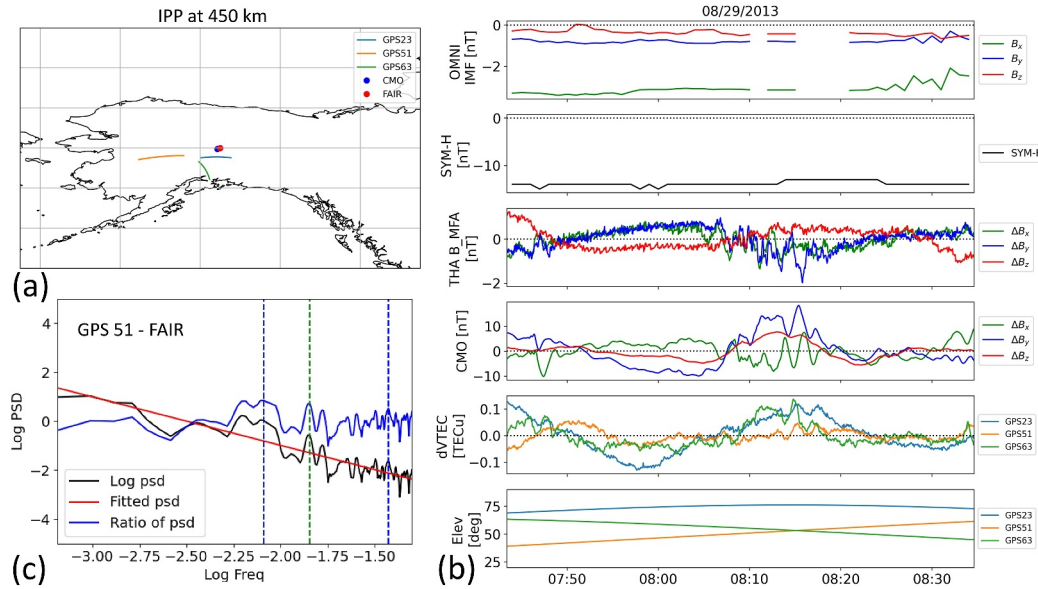

Figure 1. An example THEMIS-A satellite magnetic conjunction event on 29 August 2013 taken from the database described in Section 2.2.3. (a) The IPP at an assumed 450 km altitude (actual altitude of ULF TEC modulation may differ; if the IPP locations are at lower/higher altitude, they will cluster/further to FAIR and CMO) for the ray path from three GPS satellites to the FAIR receiver during the magnetic conjunction; the locations of FAIR and the CMO magnetometer are also shown as blue and red dots, respectively. (b) Time series stackplot during the magnetic conjunction showing the three components of Interplanetary Magnetic Field in GSM coordinates, Sym-H index, THEMIS-A satellite dBsat in field-aligned coordinates (z is parallel to the mean magnetic field, y is in the local azimuthal direction for GSM cylindrical coordinates, and x completes the right-hand orthogonal set and is directed radially outward), CMO dBground in magnetic coordinates (x is towards magnetic north, z is directed down into the Earth, and y completes the right-hand orthogonal directed roughly eastward), dTEC from the three GPS satellites-FAIR receiver pairs shown at top left, and elevation angle for the same GPS satellites. (c) The original power spectrum for dTEC from GPS 51 (black), power law fit to the power spectrum (red), and the detrended power spectrum which is equivalent to the ratio of the two power spectra (blue line). Vertical dashed lines indicate locations where peaks in the power spectra were identified, with a vertical dashed blue line indicating a common peak with a counterpart in magnetic field measurements (either satellite or ground magnetometer) and dashed green lines for peaks without counterparts in magnetic field measurements.

post-processing ensures accurate identification and characterization of significant peaks in the frequency domain analysis across different components from different instruments.

Step 3: Identify Common Peaks across Different Data Sets

To identify common peaks across different data sets in the file stored in Step 2, first any peaks identified in the CMO or THEMIS data sets with absolute power values $<10^{-2.6}\frac{nT^2}{Hz}$ are excluded from consideration to remove cases with very small amplitude waves and instrument noise (there is no corresponding threshold for dTEC wave power, see discussion at the end of Section 3.2). Next, for each peak in the TEC data (which is evaluated separately for each power spectrum) we examine whether there are any corresponding peaks in dBsat or dBground within a 4-bin frequency range (4 * 0.3255 mHz = 1.302 mHz) centered around the peak frequency. If so, the dTEC power peak is recorded as having a common peak in one or more components of dBsat (x, y, or z in field-aligned coordinates) or dBground (x, y, or z in magnetic coordinates defined earlier in this section under "Step 1"). For a single dTEC wave power peak, a common peak may occur in more than one component of dBsat or dBground; this approach is needed to support later analysis in Section 3.1 where events with both dBsat and dBground peak are examined and to avoid artificially excluding events where more than one wave mode is present (see Section 1.2). To facilitate this task, we generate survey plots showing both time series and power spectra; if such a corresponding peak is found in any component of dBsat or dBground, vertical lines representing these peaks in the survey plots are color-coded. This color-coding highlights the presence of common peaks across the different data sets, facilitating a visual identification of coinciding frequency components across the TEC data and the magnetometer or satellite data. An example of this type of survey plot is shown in Figure 1c, where three wave power peaks are identified in dTEC (blue and green dashed lines) but only two curves have a common peak in

magnetometer measurements (blue dashed lines only); the lower frequency common peak is most clearly seen and corresponds to the ∼10 mHz wave activity seen in all three time series (Figure 1b, panels 3–5 from top to bottom for dBsat, dBground, and dTEC). The higher frequency peak is much smaller amplitude and harder to discern from visual inspection of the time series; these types of very small amplitude peaks, and their possible connection in some cases to noise inherent in the measurements, will be discussed in later sections. The information on common peaks is saved to the existing database. This method represents a systematic approach to identify and analyze common wave power peaks, combining both automated event identification and validation of the automated detection via visual inspection of survey plots. This approach enables the identification of any systematic differences between wave events identified in dTEC, dBsat, and dBground.

Step 4: Inclusion of Supporting Data for Statistical Analysis

Finally, we add solar wind, geomagnetic activity indices, and THEMIS electron flux information to the existing database for each event to analyze possible drivers of identified events and their relation to different background conditions.

During the course of completing steps above, we generate a range of survey plots similar to what is shown in Figure 1 to validate the signal processing and event selection methodology. Similar to the database, these plots are made publicly available to support future investigations (Hartinger, 2024a).

2.2.4. Validation of Elevation Angle Threshold and Observing Geometry Effects

For the purpose of this study, we would like to assume that the observed dTEC is representative of the electron density variations in the ionosphere above the FAIR receiver; if we can make that assumption, then we can proceed without concern that the observing geometry significantly affects the detection of ULF wave-related dTEC. Past studies have mostly addressed this by excluding data collected when the elevation angle of the ray from the GNSS receiver to the satellite is very small, corresponding to a situation where the ray pierces the ionosphere (or altitude with dTEC modulation) further from the receiver and samples significant horizontal variation rather than variation above the receiver. However, different thresholds have been used for studying dTEC related to ULF waves, TIDs, etc., ranging from excluding data <25 to <60° (Borries et al., 2023; Watson et al., 2015), and the justification for the specific value chosen hasn't been explored quantitatively, at least for dTEC related to ULF waves which have their own unique spatial and temporal scales. Thus, before we can compare with satellite and ground-based magnetometer measurements, we quantify which elevation angle threshold is appropriate and determine what impact(s) the threshold might have on wave event detection.

As noted in the previous section, we already exclude GNSS satellite-receiver pairs when the elevation angle dips below 30° at any time during the conjunction. Figure S1 in Supporting Information S1 shows that the occurrence rate for dTEC wave events does not depend on elevation angle for all remaining GNSS dTEC time series segments (using only GPS satellites); in particular, the trend in occurrence rate versus elevation angle (mean value during conjunction event) is flat. Thus, we can proceed with examining dTEC time series with the threshold of 30° without concern that the elevation angle will affect the ability to detect dTEC events or introduce sampling biases in occurrence rates. We also examined whether the location of the IPP relative to the receiver affected the occurrence rates, and we found that it didn't; for example, the occurrence rates were the same whether the IPP was located poleward or equatorward of the receiver. This, combined with the fact that the FAIR receiver has a higher magnetic latitude (L-value) than the plasmapause in most conditions, confirms that the dTEC variations are coming from the ionosphere and not the plasmasphere (if they were coming from the plasmasphere/higher altitudes in many events, the occurrence rates should vary depending on whether the pierce point was equatorward or poleward of FAIR, with equatorward events more strongly dominated by plasmasphere contributions to dTEC). Finally, we note that these trends and thresholds would likely differ for a mid- or low-latitude GNSS receiver, and further tests would be needed in future studies at those locations.

3. Results

3.1. Wave Event Occurrence

In this section, we examine wave event occurrence versus frequency, differentiating between dTEC events with and without a counterpart in magnetic field measurements. Recall that magnetic field wave power is one diagnostic used to differentiate events driven from above and below (Section 1.2), and we checked earthquake/

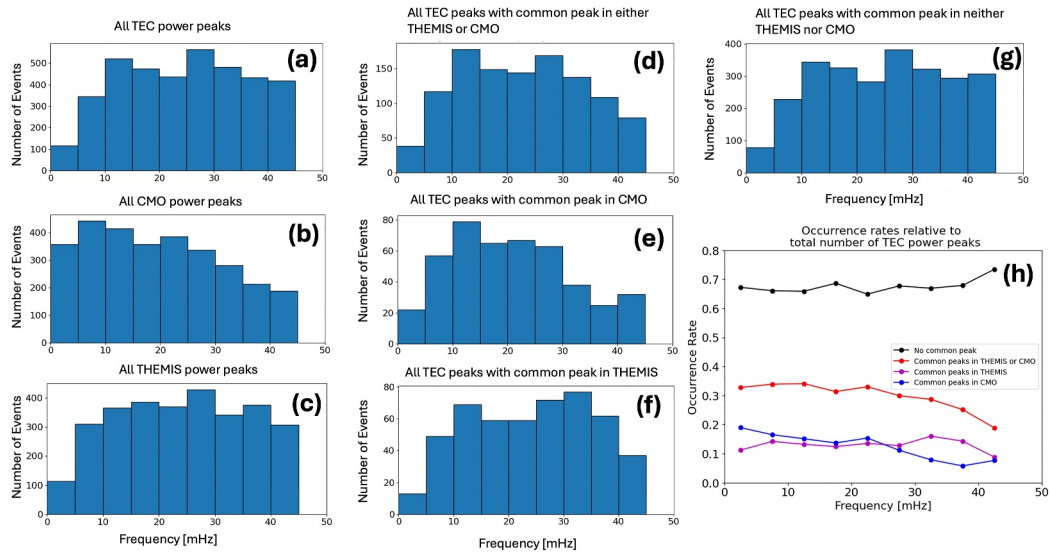

Figure 2. (a) Number dTEC power peaks versus frequency, (b) Number CMO (dBground) power peaks versus frequency, (c) Number of THEMIS (dBsat) power peaks versus frequency, (d) Number of dTEC power peaks that have a common peak in either dBground or dBsat versus frequency, (e) Number of dTEC power peaks that have a common peak in dBground versus frequency, (f) Number of dTEC power peaks that have a common peak in dBsat versus frequency, (g) Number of dTEC power peaks with no common peaks in either dBground or dBsat, (h) Occurrence rates versus frequency, where each occurrence rate corresponds to a histogram in panel (d–g) divided by the histogram in panel (a).

volcano lists during the periods analyzed in this study to rule out driving from below from earthquakes and volcanic eruptions (Section 2.1).

Figure 2 shows the number of wave events identified in detrended dTEC, dBsat, and dBground power spectra for all conjunction events as a function of frequency. Figures 2a–2c show the number of events for dTEC, dBground (CMO), and dBsat (THEMIS), respectively, as a function of frequency. The total number of events identified in the dTEC group and the dBsat/dBground groups differ; these would not generally be expected to be the same. In the case of dTEC, more than three GPS satellites may sample TEC in a single event which could potentially lead to more events being detected, whereas in the case of dBsat or dBground only three components of dB are analyzed and the measurement only comes from a single location. Note that dBsat and dBground would not generally be expected to have the same distributions since, for example, ground-based magnetometers cannot reliably remote sense all ULF wave modes, especially those with large azimuthal wave numbers (Hughes & Southwood, 1976; Shi, Baker, et al., 2018; Zhai et al., 2021).

The dTEC distribution (panel a) and the dBsat distribution (panel c, THEMIS) in Figure 2 appear very similar, with fewer events identified at the lowest frequencies ($<\sim$ 10 mHz for dTEC, $<\sim$ 5 mHz for dBsat) compared to the higher frequencies. In contrast, the distribution for dBground (panel b) has a relatively flat distribution at lower frequencies with gradually decreasing numbers of events with increasing frequency above ~25 mHz. This suggests some underlying differences between the measurements which may include the wave modes being sampled (see previous paragraph and Section 1.2), the noise inherent in each measurement, effects related to the motion of IPP/spacecraft, or some combination of several factors.

Figure 2 panels d, e, and f are all for distributions of events where peaks were identified in both dTEC and dB; panel d is for the case when waves are identified in both dTEC and either dBsat or dBground, panel e for the case where they're identified in both dTEC and dBground, and panel f for the case where they're identified in both dTEC and dBsat. In all three panels, there are relatively fewer events at low frequencies, which likely reflects the generally smaller number of events observed in dTEC at low frequencies (panel a). Additionally, there are generally fewer events at high frequencies in all three panels. This may suggest that some of the events observed at the highest frequencies ($\sim>$40 mHz) in dTEC could be artifacts since when one is observed in dTEC it isn't necessarily observed in dBsat/dBground, or vice versa. It could also relate to our definition of common peaks, in particular the distance in frequency between two peaks in dB and dTEC is fixed in absolute frequency whereas the

bandwidth of typical ULF wave events may well vary with frequency; thus our common peak definition may be too restrictive at high frequencies and miss a larger number of events relative to lower frequencies when only a slight frequency shift is present (due to, e.g., small differences in the location of the IPP and location of CMO or small Doppler shifts caused by IPP motion (Watson et al., 2015)).

Figure 2g shows a final distribution of events where peaks in dTEC have no counterpart in either dBground or dBsat. This represents several possible conditions: the event is driven from below (i.e., lower atmosphere forcing that is effective at longer wave periods, see Section 1.1), the event is driven from the magnetosphere but at another location and generates a TID that ultimately drives the observed dTEC (Pradipta et al., 2016), or some issue related to the data processing, event identification criteria, and/or different noise/uncertainties in the different measurements precludes the detection of a common wave power peak. Since nearly all previous observations and simulations of events related to surface disturbances/lower atmosphere forcing associate their corresponding dTEC variations with frequencies <5 mHz (Section 1.1), another explanation is needed for the large number of events and flat distribution at frequencies >10 mHz in panel g.

Finally, Figure 2h shows the occurrence rates for the categories shown in panels d, e, f, and g by dividing each distribution by the distribution of all dTEC power peaks shown in panel a. Several key results are seen here: (a) the category with dTEC power peaks having no counterpart in dB is the largest one with a relatively flat distribution except at the highest frequency bin, (b) fewer events are seen at higher frequencies in the categories involving dBground (CMO), (c) in general, all the occurrence rates are relatively constant with frequency for frequencies <30 mHz. The last result is somewhat surprising given certain ranges of frequencies are expected for certain ULF wave modes at FAIR's latitude, thus one might have expected a peak in occurrence near, for example, the median expected standing Alfvén wave frequency at FAIR's location (~5–15 mHz depending on magnetospheric ULF wave speeds and other factors, (Archer et al., 2015; Wild et al., 2005)). The lack of a distinct peak may be due to the mixture of several different wave modes reflected in this figure. For example, standing Alfvén waves driven by the solar wind are usually reflected in the x component of dBground or the y component of dBsat, internally driven standing Alfvén waves in y component of dBground and x or z component of dBsat, mixed and compressional modes may contribute to all three components, etc. (Section 1.2), whereas all components of dB are reflected in this figure. At the same time, different harmonics may also be present from event to event and this also isn't controlled for in this study. We return to this point in subsequent figures. Concerning (a), there may be several explanations related to lower atmosphere forcing (at low frequencies), our definition of common peaks being too restrictive and not accounting for small frequency shifts (see above), and the fact that there are more possibilities to identify dTEC events since most conjunction events have more than three GNSS satellites available for analysis.

3.2. Magnetic Local Time and Frequency Dependence of Wave Power

Next, we examine dTEC wave power versus Magnetic Local Time (MLT) at different frequencies for the category corresponding to Figure 2d (dTEC with counterpart in dB), with the time corresponding to local dawn and dusk at the FAIR site shown with dashed lines and a solid black line indicating median wave power values (note the data gap at 0 UT, near 13 MLT, due the file concatenation issue mentioned in Section 2.2.2, thus we won't emphasize fine scale spatial variations particularly at that MLT). Figure 3a shows dTEC wave power versus MLT for events in the Pc5 range (2–7 mHz), with a preference seen for large wave power near midnight (0 or 24 MLT at edges of each panel). The same trend is seen more clearly at higher frequencies, as indicated in panel b (Pc4 range, 7–22 mHz) and panel c (lower part of Pc3 range, 22–50 mHz) where a more pronounced preference for large wave power events near midnight is seen. It should be noted that when mean background VTEC is plotted versus MLT, the values are lowest near midnight (edges of panels in Figure 3) as expected in the nightside auroral zone (e.g., Themens & Jayachandran, 2016); this implies that both the largest amplitude ULF dTEC events as well as the largest relative (to background) ULF dTEC events occur on the nightside. Finally, all three panels in Figure 3 have the same y-axis range, revealing that dTEC wave power tends to decrease with increasing frequency; this same trend is shown directly in Figure S2 in Supporting Information S1, and it is consistent with other studies examining dB wave power versus frequency for ULF waves (e.g., Takahashi & Anderson, 1992).

Some of the above trends are consistent with previously reported results for the local time dependence of ULF dB power/amplitude; for example, Takahashi et al. (2012) observed elevated narrowband Pc5 wave amplitudes near midnight local time. However, some of the previously observed trends for local time dependence of dB wave

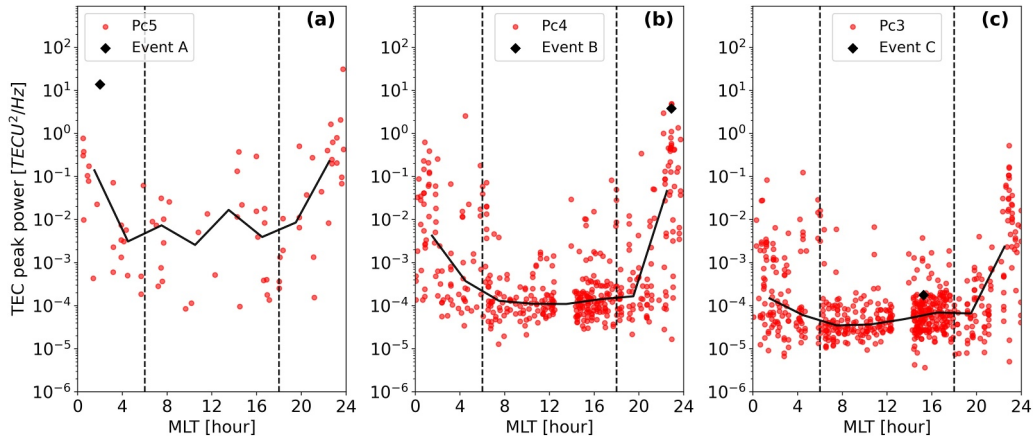

Figure 3. (a) Wave power values versus Magnetic Local Time (MLT) for peaks identified in dTEC in the Pc5 range that have a counterpart peak in either dBsat or dBground. Vertical dashed lines indicate times corresponding to local dawn and dusk. (b) The same, but for the Pc4 range. (c) The same, but for the Pc3 range. In all panels, example events shown in Figure 4 are marked with black dots with the largest peak power from each event chosen with Event A: 4.2 mHz, Pc5; Event B: 9.8 mHz, Pc4; Event C: 22.1 mHz, Pc3.

power related to ULF waves are not seen here for dTEC wave power, for example, the dawn sector preference for larger amplitude dBground wave power for narrowband Pc5 waves (Takahashi et al., 2012). This could be due in part to the mixing together of different wave modes (different components of dB are all mixed together in this Figure), each of which can have its own unique local time and frequency dependence (Cao et al., 1994; Takahashi & Anderson, 1992); it could also suggest that background ionospheric conditions that aren't directly related to magnetospheric ULF wave properties are important factors in setting dTEC amplitude.

To further explore the wave dynamics during the events represented in Figure 3, we select three example events from each frequency range as indicated by the black diamonds in the Figure; Event A is for frequency of 4.2 mHz, Event B for 9.8 mHz, and Event C for 22.1 mHz. Figure 4 shows the corresponding time series for these events, with panel A for Event A, B for Event B, and C for Event C. In each case, dTEC for all available GPS satellites are shown (i.e., if they meet the elevation angle cutoff criteria), regardless of whether they observed a wave in dTEC during the conjunction event. The red curve in Figure 4a for TEC from the GPS64 satellite represents one of the largest amplitude ULF dTEC events in the database, with a frequency of 4.2 mHz and amplitudes of $< \sim 4$ TECU in absolute terms and $\sim 30\%$ relative to background VTEC (background value not shown in Figure but was obtained from original measurements before detrending). Figure 4b is for another large amplitude dTEC event, this time with a frequency of 9.8 mHz (Pc4/Pi2 range). The event appears very similar to typical dTEC events with step-like increases identified in Watson et al. (2011) who focused on TEC variations related to substorm particle precipitation. Precipitation did indeed occur during this event, as seen by an auroral activation shown in Movie S1. In this event, multiple frequencies were observed in dTEC, though the 9.8 mHz frequency is most consistently seen during the whole interval - note the $\sim$10 mHz variations seen in, for example, the red curve well before the step-like increase occurs. Movie S1 and related keograms (not shown) also indicate similar period wave activity was seen in the aurora before, during, and after the activation.

Figure 4c is for an example event in the Pc3 frequency range at 22.1 mHz (just above the Pc4 range). Waves with periods less than a minute can be seen in all curves (note these are the smaller amplitude waves superposed on longer period, larger amplitude, and irregular wave activity), with this wave activity having the largest amplitude near the end of the interval. This event highlights (a) the sensitivity of dTEC to even very small amplitude variations ($\sim <$ 0.05 TECU amplitude) and (b) the challenge in assigning a noise floor to dTEC. Although the wave power in the frequency domain is small and appears clustered with a large number of other small wave power events in Figure 3c, suggestive of a noise floor to the dTEC measurement, the time domain analysis reveals clear wave activity in multiple GPS satellites. Moreover, the same frequency wave activity is also observed in magnetometer measurements, a completely different instrument with different noise characteristics. This is true for many of the other events with low wave power in Figure 3, and it suggests (a) that dTEC can be used to detect very small amplitude wave-like dTEC variations and (b) that more work is needed to rigorously identify a noise

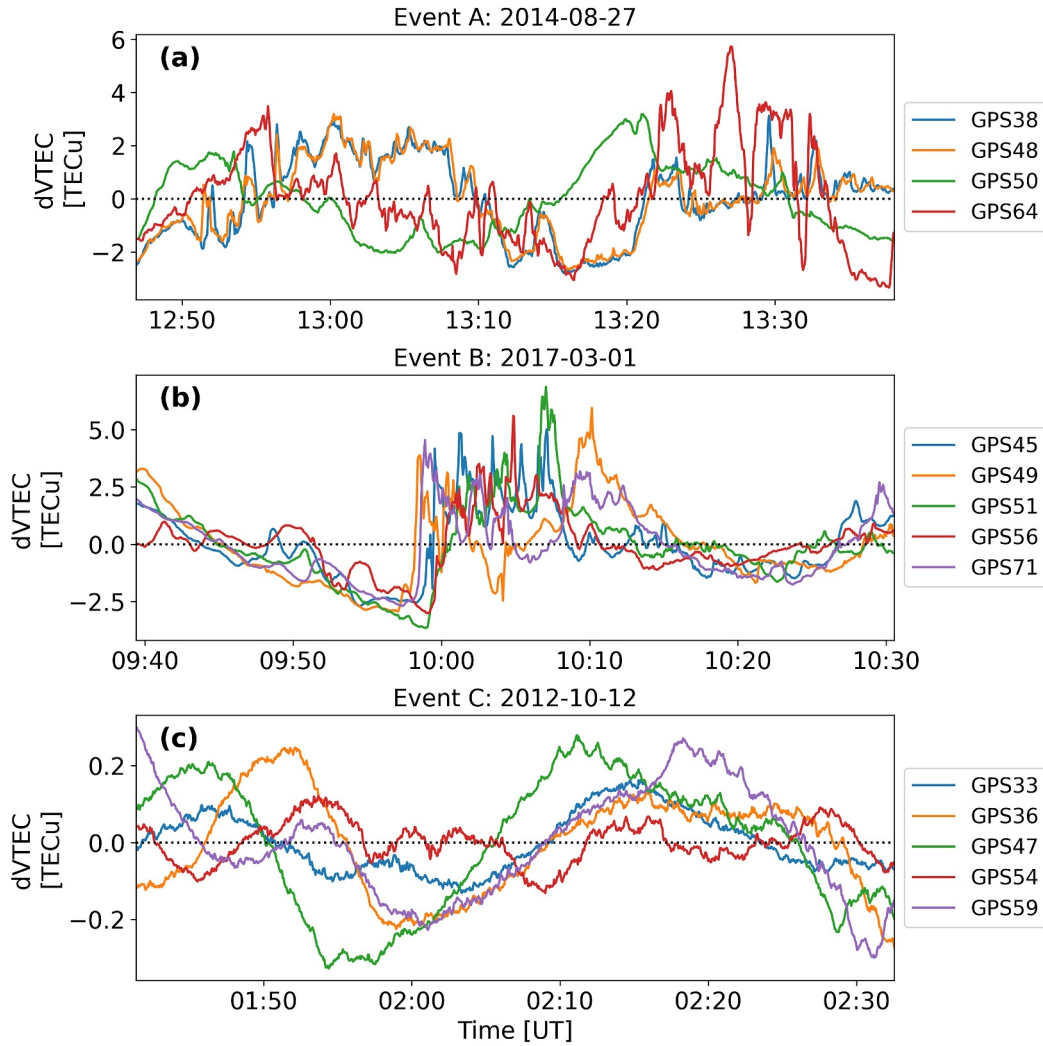

Figure 4. dTEC time series corresponding to case studies indicated by the black dots in Figure 3. Each panel is for a different event, with dTEC shown for all available GPS satellites (that meet elevation angle criteria and data quality checks) regardless of whether they identified a wave power peak.

floor for dTEC that takes into account the many stages in the data processing pipeline related to biases in STEC, conversion to VTEC, event-specific GPS satellite motion, etc.

3.3. Relationship Between dTEC Wave Power and Driving Condition

Next, we examine what factors control ULF dTEC for those events that have a counterpart in dBsat or dBground. Figure 5 shows the peak dTEC PSD for dTEC wave events as a function of solar wind speed (top row), AE index (middle row), and Kp index (bottom row), with red lines representing least squares fits of the logarithm of dTEC wave power to the logarithm of solar wind speed, logarithm of AE, and Kp. Figure 5a shows the dTEC PSD for events in the Pc5 band versus solar wind speed, following many other studies that established a correlation between Pc5 dB (satellite and ground) and solar wind speed related to surface waves on a Kelvin-Helmholtz (K-H) unstable magnetopause (e.g., Engebretson et al., 1998; Mathie & Mann, 2001; Takahashi & Ukhorskiy, 2007). Similar to these studies, larger dTEC wave power is observed at larger solar wind speeds; the trend would likely be more evident if there were sufficient events to limit analysis to flank regions (Engebretson et al., 1998). However, it is not necessarily expected that the same correlations would be found between dTEC power and solar wind speed since many other factors control dTEC amplitudes. For example, even if magnetopause surface waves related to the K-H instability are responsible for both increased dB and dTEC amplitudes, the dependencies of

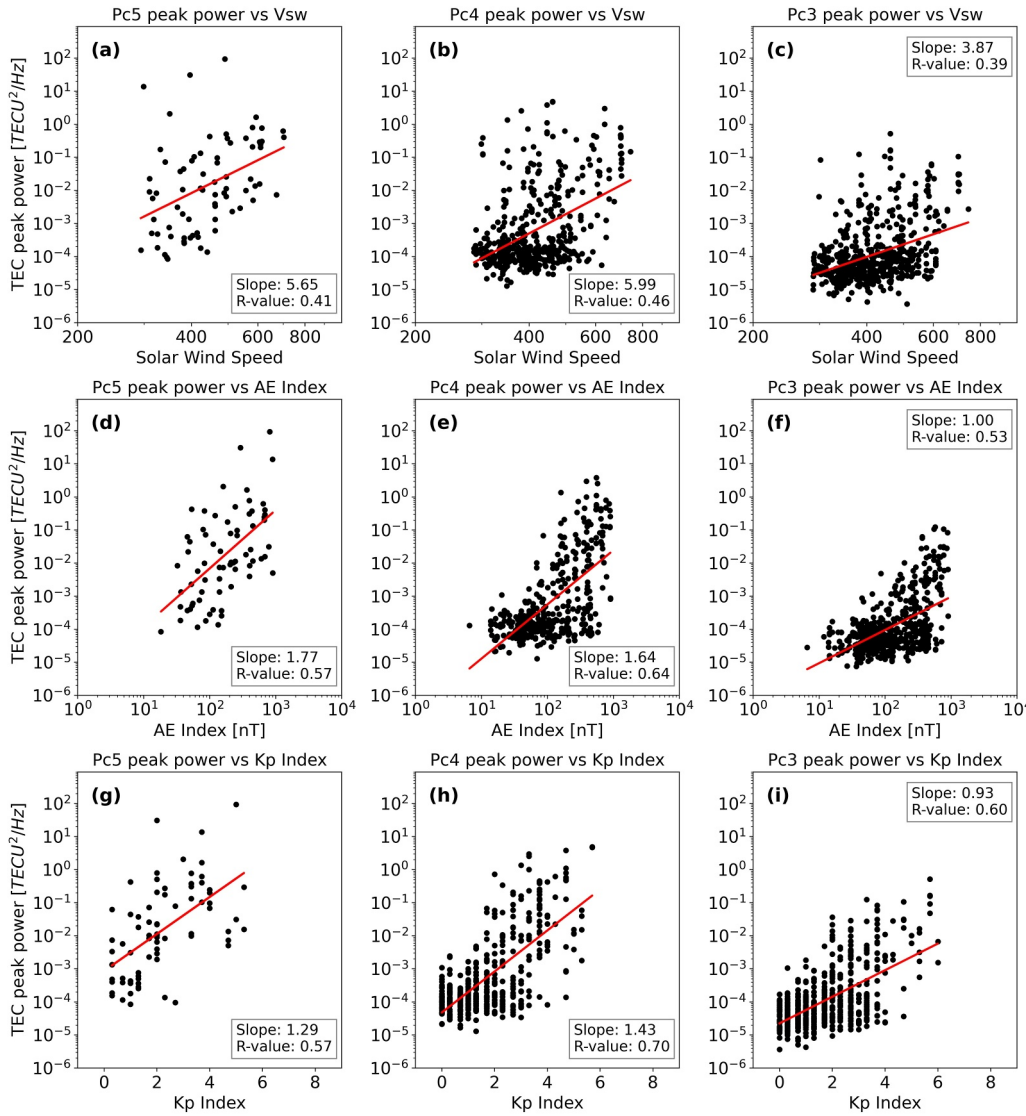

Figure 5. dTEC wave power in different frequency bands versus solar wind and geomagnetic activity indices. (a–c) Pc5 (2–7 mHz) dTEC power versus solar wind speed (a), AE index (b), and Kp index (c). (d–f) Pc4 (7–22 mHz) dTEC power versus solar wind speed (d), AE index (e), and Kp index (f). (g–i) Pc3 (22–100 mHz) dTEC power versus solar wind speed (g), AE index (h), and Kp index (i). In all panels, red lines are for least squares fits with corresponding slopes and R-values shown in the inset.

these two parameters would be different with, for example, dTEC potentially more sensitive to background ionospheric conditions. This may explain the lower R-value in panel a compared to results from past studies of dBground at similar magnetic latitudes (Engebretson et al., 1998; Mathie & Mann, 2001), where R-values closer to ∼0.6–0.8 are found for different magnetic latitudes, though it's intriguing to note that other studies examining dBsat found a wider range of R-values, including values as low as ∼0.3 depending on the specific region examined (Takahashi & Ukhorskiy, 2007). Figures 5b and 5c are for the Pc4 and Pc3 bands, respectively. The R-values for these frequency bands (0.46 and 0.39) are similar to the Pc5 band (0.41).

Panels d, e, and f in Figure 5 are for correlations between dTEC wave power and the AE index in the Pc5, Pc4, and Pc3 frequency bands, respectively. The AE index has been linked to elevated ULF wave power in the nightside magnetosphere related to substorm activity and wave-particle interactions caused by particle injections. This is particularly true in the Pc4-5 (or Pi2, 7–22 mHz) frequency range (e.g., Shi, Ruohoniemi, et al., 2018). In panels d,

e, and f, a correlation is observed between AE and dTEC wave power in all three frequency bands, suggesting a similar connection with substorms/particle injections.

Finally, panels g, h, and i in Figure 5 show correlations between dTEC wave power and the Kp index in the Pc5, Pc4, and Pc3 frequency ranges, respectively. Kp has been linked to elevated ULF wave activity in dB across a broad range of frequencies in numerous past studies (e.g., Takahashi & Anderson, 1992), and this is consistent with the trend of large amplitude waves occurring during periods with elevated geomagnetic activity. Here, again, similar trends are observed in dTEC wave power, with the same caveats as the other panels in Figure 5 that some factors that explain the correlation between dTEC and Kp may differ with the factors that explain the correlation between dB and Kp, though the R-values shown in panels g, h, and i are at least consistent with past studies of dBsat (Takahashi & Anderson, 1992). It should also be noted that, as seen in Figure 5, there are no dTEC samples at large Kp/major geomagnetic storms; this reflects the sampling bias mentioned in Section 2.2.1. Given the trend for increasing dTEC amplitude with increasing Kp, this suggests that the largest dTEC amplitudes in this study are smaller than those that might be expected to occur during major geomagnetic storms. Figure S3 in Supporting Information S1 shows a similar trend with increasing dTEC power versus the absolute value of the Sym-H index, another index representing geomagnetic storm and ring current intensity.

Taken together, the results of Figure 5 indicate that dTEC ULF wave power is well correlated with similar parameters as dB ULF wave power. These are dTEC events that have already been linked to magnetospheric ULF wave activity in the form of common peaks with dBsat or dBground, thus it may not be surprising to see similar correlations in dTEC as in dB. However, this need not have been the case. Had other factors related to ionospheric or atmospheric background conditions predominately controlled the dTEC amplitude for these events, weak or no correlations may well have been observed. The fact that Figure 5 reveals correlations with parameters that are consistent with dB suggests that large dTEC amplitudes can in large part be predicted by the same factors as for large dB amplitudes. We continue to explore this in the next section.

Finally, recall that Surkov et al. (2023) and other past studies have shown that lower atmosphere forcing (earthquakes, volcanic eruptions) can lead to dB in the Pc5 range or at lower frequencies. Although we have already checked volcano and earthquake lists and found no major events in close proximity (time or space) to the events considered in this statistical study, Figure 5 provides further evidence that many of the dTEC events are not related to lower atmosphere forcing (including other sources not considered in the lists such as terrestrial weather). In particular, if the events had been mostly associated with lower atmosphere forcing, it would be highly implausible to see correlations with solar wind speed, AE index, or Kp index since none of these parameters have correspondence with the timing of volcanic eruptions, magnitude of earthquakes, etc. However, it is likely that some of the dTEC events examined in Figure 5 are related to lower atmosphere forcing. Moreover, even in events related to driving by magnetospheric ULF waves, lower atmosphere forcing may have occurred at the same time as the ULF waves. Thus, lower atmosphere forcing is likely a source of scatter (i.e., leads to weaker correlations) in the results shown in Figure 5.

3.4. Relationship Between dTEC Wave Power and Magnetic Field Wave Power

In this section, we focus on the subset of dTEC events with a counterpart wave power peak in dBsat or dBground, and we examine how magnetospheric ULF wave properties and conditions affect dTEC wave power. Figure 6a shows dTEC peak wave power versus dBground peak wave power, where different colors/symbols indicate the component of the magnetic field measured by the ground magnetometer. A positive correlation is seen between the magnetic field and dTEC wave power: as magnetic field wave power increases, so to does dTEC wave power. However, there is scatter in the data (reflected in the R-values shown in the inset). This is due at least partly to the different factors controlling dB and dTEC. For example, the dTEC wave power for a given slant path (ray from FAIR to GNSS satellite) depends on how the slant path pierces the ionosphere and the altitude of strongest ULF electron density modulation. The scatter is also likely due to the different mechanisms that connect magnetospheric ULF waves to dTEC in any given event. Additionally, there is a noticeable flattening of the trend at low wave power (bottom left of plot). This may be due to some of these events being close to the noise floor of the dTEC measurements (note we already remove low signal events in dBground, this leads to the abrupt cutoff in events in the left part of panel a); as noted in discussion related to Figures 3 and 4c, determining the noise floor of dTEC is complicated and depends on several factors that may vary from event to event, thus we don't exclude events with low dTEC power. This flattening may also be due to the fact that low dTEC and dB wave power

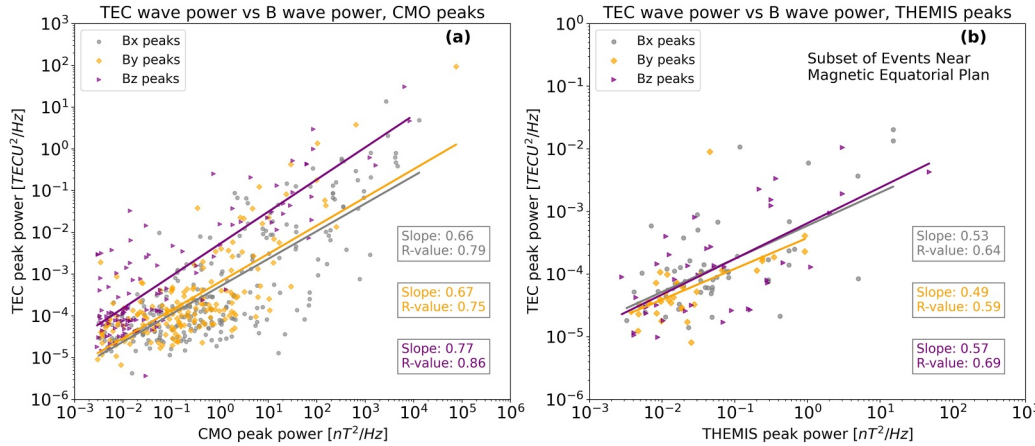

Figure 6. (a) dTEC peak wave power versus dBground peak wave power for events with a common peak, where color indicates the component of the magnetic field where x is towards magnetic north, z is directed down into the Earth, and y completes the right-hand orthogonal set (roughly eastward). (b) The same as panel (a), but for dBsat in FAC where z is parallel to the mean B, y is in the local azimuthal direction for SM cylindrical coordinates, and x completes the right-hand orthogonal set and is directed radially outward. Additionally, only events where the observing satellite is located close to the magnetic equatorial plane $\left(\frac{B_zGSM}{|B|} > 0.95\right)$ are shown to remove effects related to field-aligned mode structure (see text). In both panels, lines are for least squares fits where color again indicates component of the magnetic field; corresponding slopes and R-values are shown in the insets.

events tend to correspond to higher frequency waves, and these waves may not have as strong a correspondence between dB and dTEC. This is confirmed in Figure S4 in Supporting Information S1, which shows the same results but split according to Pc5, Pc4, and Pc3 frequencies.

Somewhat different trends are seen in the different magnetic field components (colors/symbols) in Figure 6a. Although all three colors exhibit a correlation between dTEC and dBground, there is somewhat less scatter in the vertical (z) component compared to the other components as reflected in the differing R-values. Moreover, the dTEC wave power tends to be higher for the z component events compared to events for other components of the magnetic field (purple dots and line tend to be above dots for other colors). Past observational studies have linked the z component of dBground to field-aligned currents and waves (e.g., Clauer & Ridley, 1995; Lanzerotti et al., 1990), though as noted in Section 1.2 this component may be associated with more than one ULF wave mode, effects of localized wave activity, and/or spatially inhomogeneous ionospheric or ground conductivity. Pilipenko, Belakhovsky, Murr, et al. (2014) proposed that field-aligned current transported by Alfvén waves (such as toroidal or poloidal modes) could cause a ULF dTEC modulation (Section 4.7 in that study). If this is true for the events shown in Figure 6, the fact that dTEC amplitudes most strongly correlate with the dBground z component (vertical, directed into the Earth) could be due to the fact this component most closely represents field-aligned current related to Alfvén waves: disturbances in the z component are largest when CMO is in close proximity to regions with large wave-related field-aligned current variations (e.g., Clauer & Ridley, 1995; Lanzerotti et al., 1990), thus large current-related variations in electron density (dTEC) (Pilipenko, Belakhovsky, Murr, et al., 2014). Regardless, the data shown in Figure 6a show a quantitatively different trend in the z component compared to the other two components that should be studied further with additional data and modeling that can isolate the role of specific ULF wave modes, localized wave activity, and inhomogeneities in ionospheric or ground conductivity in producing ULF dTEC and dBground.

Figure 6b is the same format as 6a, but for dBsat instead of dBground. Additionally, we use the measured magnetic field averaged over the conjunction interval to limit to events when the satellite is close to the magnetic equatorial plane using the test $\frac{B_{zGSM}}{|B|} > 0.95$. This data reduction step is necessary as we are now comparing dTEC power to satellite wave power, and the satellite wave power depends in part on the interplay between wave harmonic mode structure along a field line and the satellite location in this structure. By limiting to the magnetic equatorial region, we reduce this source of scatter in the measurements for a more direct comparison with the ground magnetometer results (unlike the satellite which has a variable location relative to the magnetic equator,

the ground magnetometer is always fixed underneath the ionospheric footpoint of the wave field). After applying this data reduction step, the correspondence between dBsat and dTEC is seen in Figure 6b, with events at higher THEMIS peak power tending to have higher dTEC power, consistent with the ground magnetometer results on the left. Unlike the ground magnetometer, there aren't any major differences between the trends for different components of dBsat (note the similarity in the slopes, R-values, and location of the curves on the chart, in contrast to Figure 6a). Also different from the ground magnetometer, the R-values and slopes are overall smaller, likely due to scatter related to (a) the satellite's variable location relative to the magnetic equator which cannot be completely removed with the data reduction step listed above and (b) uncertainty in the magnetic field-line tracing from the satellite to the ground (Section 2.2.1). For completeness, the full set of conjunctions is shown in Figure S5 in Supporting Information S1; significantly more scatter is present in these results due to the harmonic mode structure effect mentioned above. Figure S6 in Supporting Information S1 also shows the same results split according to Pc5, Pc4, and Pc3 frequencies as was done for the ground magnetometer in Figure S4 in Supporting Information S1.

4. Discussion

4.1. Summary of Results and Relation to Previous Work

4.1.1. Wave Event Occurrence

The results shown in Figures 2 and 3 reveal new information about how ULF dTEC and dB event detection varies according to frequency for events with and without magnetic signatures. As discussed in Section 3.1, the frequency dependence of the occurrence rate depends on the category of event under consideration; occurrence rates for dTEC waves without a counterpart in dB are relatively flat for the frequency range under consideration (∼2–45 mHz). This is surprising for the higher frequency events, since past studies usually associate a lack of signal in dB as evidence for dTEC driven from below, yet sources of ULF dTEC from gravity waves/driving from below should occur at frequencies $<\sim 5$ mHz (Section 1.1); having dTEC frequencies up to 45 mHz suggests a magnetospheric source, but evidently something precludes the detection of a magnetic signature in these events. Future work should identify the source(s) of these dTEC events and determine whether a magnetic signature is expected and, if so, why it isn't detected (e.g., due to frequency shifts between dB and dTEC related to IPP location and/or motion (Watson et al., 2015)).

Figure 3 shows further information about the frequency dependence of wave power/amplitude for dTEC events with a magnetic counterpart. In particular, as is the case for ULF waves observed in magnetic field, the wave power generally decreases with increasing frequency. Evidently, the decreased wave power at higher frequencies does not significantly impact the occurrence rates (compare with Figure 2). Figure 4 shows example time series corresponding to both large and small dTEC amplitude events seen in Figure 3. These events have a range of amplitudes that are consistent with past studies that found a large range of dTEC (∼0.05–7 TECU) and dTEC/TEC amplitudes (∼0.002–0.35, Pilipenko, Belakhovsky, Murr, et al., 2014; Watson et al., 2015). They are also comparable to dTEC related to TIDs caused by driving from below (Heki, 2021; Meng et al., 2019).

Figure 3 also shows the distribution of dTEC events with a magnetic counterpart versus MLT. Across all frequencies there's a notable increase in wave power near midnight. This may suggest that background ionospheric conditions play an important role in determining dTEC amplitudes, with nightside conditions tending to lead to larger amplitudes, or that processes occurring on the nightside such as particle injections play a prominent role in determining dTEC amplitude. More work is needed to understand these results, though it is already clear from this figure that some MLT dependencies observed previously for magnetospheric ULF waves in dB do not appear as strongly in dTEC (Takahashi et al., 2012). At least two other studies have examined MLT dependences of dTEC, though at different magnetic latitudes than FAIR and using somewhat different analysis approaches. Watson et al. (2016a) examined dTEC in the polar cap (magnetic latitudes >74° in contrast to FAIR's magnetic latitude of 65.46°) and did not require a counterpart signature in dB, generally finding larger occurrence rates and amplitudes on the dayside though with the specific MLT dependence varying according to magnetic latitude. Okuzawa and Davies (1981) examined dTEC with frequencies of 20–100 mHz (Pc3-4) at a magnetic latitude of roughly 48°, finding more events on the dayside/post-noon. Thus, it may well be the case that the MLT dependence indicated in Figure 3 for auroral zone latitudes does not generalize to other latitudes.

4.1.2. Wave Power Dependencies

We find results in Figure 5 that are generally consistent with past studies, with dTEC power at all frequencies exhibiting a strong correlation with the Kp and AE indices, consistent with past studies of ULF wave dB (Takahashi & Anderson, 1992) and ionospheric electric field (Shi, Ruohoniemi, et al., 2018) in the auroral zone that also found correlations across a wide range of frequencies. dTEC power and solar wind speed are also correlated, though with R-values from least squares fits generally at the lower range of values found for past observational studies of dB power and solar wind speed (Engebretson et al., 1998; Mathie & Mann, 2001; Takahashi & Ukhorskiy, 2007). These results provide the first statistical evidence that similar trends observed in ULF dB are also observed in ULF dTEC. They also imply that future efforts to predict ULF dTEC amplitude using global indices or solar wind drivers would be successful, though more research is needed to determine which parameters best predict ULF dTEC as has already been done for dB (e.g., Bentley et al., 2020).

Another key result in this work relates to the correspondence between the dTEC and dB amplitudes. As shown in Figure 6a, dTEC wave power correlates well with dB wave power, at least for a ground magnetometer that's not subject to the field line tracing and satellite motion issues discussed in Section 3.4. This result suggests the two are linked, though there was no reason to expect such a strong correlation prior to this study. It could have transpired that background ionospheric or magnetospheric conditions play the dominant role in controlling the dTEC amplitude, with the magnetospheric ULF wave amplitude (represented by dBsat or dBground) playing a secondary role. For example, this may have occurred if proximity to large horizontal ionospheric electron density gradients (e.g., edge of auroral oval) or the presence of large magnetospheric field-aligned electron populations were the primary factors setting the dTEC amplitude. Figure 6 also demonstrates that some components of the magnetic field correlate with dTEC power and occurrence better than others. For example, the R-value for the power-law fit between the z component (vertical, into the ground) of dBground and dTEC is much larger than for other components of dBground or dBsat; regardless of the physical mechanism causing this difference, this result indicates that the z component of dBground is the best proxy for dTEC and vice versa (see Section 4.2 for implications for remote sensing). Moreover, the differing power law slopes shown in Figure 6 inset as well as the differing offsets (especially for the z component of dBground, note the shift between the purple line and other lines in Figure 6a) indicate there may be different underlying physical mechanisms controlling the relationship between dTEC and different components of dBground and dBsat. In particular, the larger slope and offset for the z component of dBground indicates it is related to dTEC via a higher order polynomial with larger scale factor compared to the other components of dBground and dBsat. As described in Section 3.4, we speculate this may indicate a connection between the vertical component of dBground, Alfvén wave field-aligned current, and dTEC following the mechanism proposed by Pilipenko, Belakhovsky, Murr, et al. (2014), though this would need to be tested in future studies with methodology to identify specific wave modes, etc. Finally, past studies including Pilipenko, Belakhovsky, Murr, et al. (2014) and Watson et al. (2015) reported the ratio of the dTEC/dBground, finding values ranging from ~0.002 to 0.1–0.7. These numbers are within the scatter in Figure 6, but clearly they depend on the component of the magnetic field being measured, with the ratio consistently higher for the z component. This ratio could be a useful diagnostic of the specific mechanisms connecting dB and dTEC, as already suggested by these studies.

Taken together, the results of this statistical analysis suggest that, at least in the auroral zone, (a) there is a notable connection between dTEC and magnetospheric ULF wave properties and (b) many factors contribute to the observed dTEC since the ULF waves and ionospheric electron density disturbances are connected by a long set of coupled processes. The processes connecting ULF waves and dTEC can vary from event to event and location to location as different mechanisms come into play. For this reason, one shouldn't expect a one-to-one correspondence between wave amplitudes observed in the magnetosphere, remote sensed with a ground magnetometer, or remote sensed with dTEC in a study that mixes together all wave modes, ionospheric conditions, etc. Follow on studies could isolate specific mechanisms linking magnetospheric ULF waves (dBsat and dBground) to dTEC to further examine what factors most strongly control dTEC amplitude. Figure S7 in Supporting Information S1 illustrates one example of a possible type of future analysis using the database created in this study by exploring the connection between electron precipitation and dTEC. Electron precipitation is one source of dTEC variations related to magnetospheric ULF waves (Shen et al., 2024), as discussed in Section 1 and shown in the example of Movie S1 (Event B in Figure 4). In Figure S7 in Supporting Information S1, a proxy for the available population of electrons for precipitation is compared to dTEC wave power, with a relatively weak correlation found. The weak correlation could be due to the limitations of the proxy, in particular the fact there are many

sources of electron precipitation with different energy ranges, local time dependence, relation to ambient conditions, etc. Thus, more work is needed to develop proxies suitable for whistler mode wave-related precipitation, precipitation related to the large-scale ULF wave field-aligned current, and other sources of precipitation modulated by ULF waves to understand and quantify the role of precipitation in generating dTEC.

4.2. Implications of the Results

4.2.1. Remote Sensing

As noted in Section 1, remote sensing techniques for magnetospheric ULF wave fields are needed for many space weather applications, including for quantifying radial transport rates in radiation belt and ring current models. Ground-based magnetometer and satellite measurements are already used for this application, but they suffer from significant gaps in spatial coverage and, in the case of ground magnetometers, they cannot detect certain ULF wave modes that are screened by the ionosphere (Hughes & Southwood, 1976). dTEC obtained from GNSS receivers has been proposed as a complementary tool for remote sensing magnetospheric ULF wave properties, and it has been used successfully in case studies to remote sense wave properties (Watson et al., 2015), including for waves that are screened by the ionosphere and not clearly observable in ground magnetometer data (Zhai et al., 2021). There is also little doubt that the addition of GNSS receivers would improve spatial coverage of ULF wave observations, given their dense spatial coverage, including in regions with few ground magnetometers (e.g., West Antarctica, (Alfonsi et al., 2022)) and potential for coverage over oceans via buoy networks (Azeem et al., 2020). However, no previous studies have established a statistical connection between ULF wave amplitudes observed in dB and dTEC needed to use dTEC amplitude as a proxy for dB amplitude, and there is some doubt whether such a connection exists given the range of potential mechanisms for driving ULF dTEC (Pilipenko, Belakhovsky, Murr, et al., 2014) and the range of $\frac{dTEC}{dB}$ values obtained in past case studies (Watson et al., 2015).

The results shown in Figures 5 and 6 have established a clear connection between ULF wave power observed in dBground and dTEC, suggesting dTEC measurements could supplement dB measurements to fill in gaps in spatial coverage for the purpose of obtaining global ULF wave observations, at least for certain applications. For example, event-specific ULF wave fields obtained from ground magnetometers perform better than wave power obtained from empirical models; Murphy et al. (2016) found that empirical models based on Kp can differ from event-specific wave power by several orders of magnitude. Thus, for this application using dTEC to estimate event-specific dB wave amplitudes to within an order of magnitude would be an improvement from estimates from empirical models which can be off by several orders of magnitude. The scatter (quantitatively represented by R-values) seen in Figure 6 indicates that dTEC should be adequate for the purpose of roughly estimating ULF wave power in a region with few magnetometer observations available. It's also likely that with further statistical analysis dTEC could perform much better as a predictor of dB. The results in Figure 6 are only a first step as they include all frequencies, components of dB, elevation angles, etc; it is highly likely that further work focused on determining what factors lead to the best correspondence between dB and dTEC amplitudes at different frequencies, for different wave modes, etc. would be successful.

Beyond estimates of wave amplitude, dTEC should also be adequate for estimating magnetospheric ULF wave frequency. This has already been established statistically at mid-latitudes over a several month sampling interval (Okuzawa & Davies, 1981), and this study extends the result to auroral zone latitudes and a larger time range. dTEC may also be useful for estimating wave spatial structure, phase speed, and other parameters as was done in Watson et al. (2015) and Zhai et al. (2021), though this would likely involve the use of additional GNSS receivers. We examined measurements from a single receiver in this study, but the analysis can easily be extended by involving multiple GNSS receivers in a follow-on study.

To illustrate the points discussed in this section, we performed a numerical simulation of ULF dTEC in a realistic 3D ionosphere-thermosphere system using the Global Ionosphere Thermosphere Model (GITM) as has been done for past studies focused on driving from below from, for example, earthquakes (Meng et al., 2018) and driving from above by ionospheric electric field variations (Meng et al., 2016, 2022). In particular, we impose a large scale, 10 min period ULF electric field variation on the ionosphere, then extract the integrated electron density along several lines of sight from a virtual receiver located in the auroral zone to virtual satellites. The top left and bottom left of Figure 7 shows the location of several lines of sight that pierce the 3D ionosphere at different

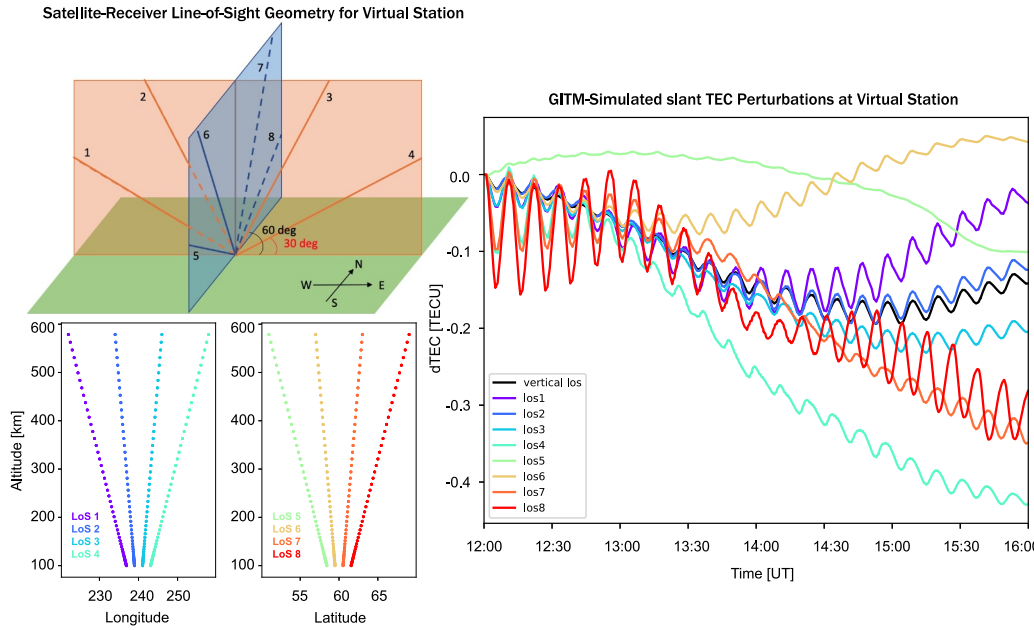

Figure 7. Results from a numerical simulation of dTEC related to a ULF wave event. (Top left) Line of sight trajectories for extracting virtual dTEC from the simulation. (Bottom left) Additional information about the latitude, longitude, and altitude dependences of the lines of sight for extracting dTEC from the simulation. (Right) Simulated dTEC for a ULF wave event from a single receiver. Color indicates different lines of sight indicated in the left part of the figure.

locations in latitude and longitude. On the right part of the Figure, virtual dTEC is shown for these different lines of sight, where a standard mapping factor is applied to estimate the vertical dTEC, as would be done if this was an observational case study (e.g., Mannucci et al., 1998). Finally, the vertical dTEC extracted from the simulation is shown as a black line. Clearly, there are considerable differences from one line of sight to another, with dTEC amplitude and phase varying according to where the line of sight pierces the ionosphere. However, the frequency does not vary considerably, and a wave event is detectable in all time series. The same patterns can be seen in the examples of Figures 1 and 4 (particularly Events B and C). This supports the points made in this section, and it further shows that while observing geometry does not affect the ability to detect wave activity in TEC or significantly alter wave frequency (Section 2.2.4), it does affect phase and amplitude somewhat. This further suggests that some of the scatter seen in Figure 6 is due to observing geometry that varies from event to event, and thus may be reduced if, for example, only events with very high elevation angles are included; exploring the role of elevation angle would be a logical next step for any future study seeking to improve ULF wave amplitude remote sensing capabilities. Figure 7 also suggests that spatial averaging of dTEC from multiple time series, a practice sometimes used to obtain global TEC maps with finite latitude/longitude resolution, would tend to average out contributions to dTEC from magnetospheric ULF wave activity. Thus, these maps would not generally be appropriate for ULF wave remote sensing applications unless, for example, spatial resolutions are much smaller than typical ULF wavelengths in the ionosphere.

4.2.2. Magnetosphere-Ionosphere Coupling and Space Weather Impacts

The results shown in Figure 3 and the case studies in the top two panels of Figure 4 present a challenge to our understanding of M-I coupling related to ULF waves and other processes. These results suggest that the large amplitude ULF dTEC events found in past case studies (Pilipenko, Belakhovsky, Murr, et al., 2014; Watson et al., 2015) are not unique. Taken together with the fact that these events tend to occur in a background of relatively small TEC values on the nightside, these events represent significant disturbances to background TEC of up to $\sim 30 - 40\%$. In contrast, nearly all ULF wave models assume a static ionosphere with at most small (linear) disturbances in ionospheric parameters related to the waves, including electron density and ionospheric conductance (e.g., Lysak & Lee, 1992), and the same assumption is routinely used for remote sensing magnetospheric ULF wave fields with ground magnetometer measurements (Ozeke et al., 2009). Regardless of whether these variations in TEC represent net increases to background ionospheric electron density over the duration of an

event, back and forth motion of plasma with no net change, etc., these large amplitude events are not consistent with the assumptions used in most models and theory to describe auroral zone ULF wave activity. Pilipenko, Belakhovsky, Kozlovsky, et al. (2014) showed in a case study using ISR measurements that large variations (up to 60%) in ionospheric parameters resulted in a "non-linear distortion" of the ULF waveform observed with ground magnetometers, inconsistent with predictions from linear theory. As discussed by Wang et al. (2020) in the context of a case study using ISR measurements, linear theory may not be adequate to describe these large disturbances, with implications for wave reflection coefficients and overall dynamics, ionosphere-thermosphere heating rates, and wave dissipation rates. Follow on studies should examine case studies of these large dTEC/TEC events to determine if linear theory is adequate to describe the spatial/temporal evolution of these waves. This is facilitated by the database and corresponding survey plots showing both dTEC and dB that were constructed as part of this study (Hartinger, 2024a, 2024b).

ULF dTEC can lead to several types of space weather impacts as noted in Section 1. For example, as shown by Wang et al. (2020) with PFISR observations, large changes in ionospheric conductance are possible in the presence of the largest amplitude dTEC variations shown in Figures 3 and 4. This could affect a host of other auroral zone processes that are controlled in part by ionospheric conductance, including ionospheric heating and geomagnetic disturbance related to geomagnetically induced currents. The large amplitude dTEC events found in this study motivate the need for several future studies focused on space weather impacts. For example, Joule heating rates and conductances could be estimated using PFISR for both large and small amplitude dTEC events using the database obtained in this study (Hartinger, 2024b). As another example, the effect of large dTEC variations on geomagnetic disturbance could be examined by statistical analysis of CMO observations for both the large and small amplitude dTEC events obtained in this study. Finally, given the fact that the results in this study are biased to weak to moderately active geomagnetic activity conditions (Section 2.2.1, no dTEC samples at large Kp in Figure 5), and given the trends in Figure 5, it is highly likely that significantly larger dTEC amplitudes are possible than were reported in this study; thus, additional studies are needed of dTEC during major geomagnetic storms to determine a more realistic upper bound for dTEC amplitudes and better assess their significance to space weather.

In addition to large TEC conductance variations, ULF dTEC variations may also lead to scintillation through, for example, precipitation that leads to ionospheric irregularities (Kim et al., 2014; Shen et al., 2024; Tsunoda, 1988; Yizengaw et al., 2018). More work is also needed to determine whether this is a common occurrence and, if so, when/where it occurs.

5. Summary

In this study, we used ∼<3s TEC measurements from the FAIR GNSS receiver in a statistical study of dTEC in the auroral zone supported by ∼7 years of THEMIS satellite measurements as well as the CMO ground magnetometer. We find several key results related to the questions posed at the end of Section 1:

1. In the auroral zone, monochromatic (i.e., with discrete frequency peak in the power spectrum) magnetospheric ULF waves drive Total Electron Content (TEC) variations with frequencies of ∼2–50 mHz and amplitudes correlated with Kp, AE, and solar wind speed to varying degrees for different wave frequencies. This is qualitatively consistent with past studies examining correlations between ULF dB and the same parameters.
2. dTEC amplitude is well correlated with ground and satellite magnetic variation amplitude, though the correlation depends on magnetic field component.
3. The largest amplitude dTEC events have amplitudes of $< \sim 4$ TECU and ∼30% of background TEC and occur most often near local midnight and at frequencies $< \sim 7$ mHz.

The results of this study strongly suggest that dTEC would be a useful proxy for magnetospheric ULF wave frequency and amplitude for some applications (e.g., for obtaining event-specific radial diffusion coefficients for radiation belt/ring current models). The large dTEC and dTEC/TEC amplitudes found in this study suggest potentially important impacts on magnetosphere-ionosphere coupling processes that would not be captured in theory/models assuming static ionospheric conductance/linear ionospheric disturbances, though more work is needed to quantify impacts on ionospheric conductance, geomagnetic disturbance, etc. More work is also needed to determine at what altitude the modulation of dTEC occurs for different categories of events/different wave modes, how the results found in this auroral zone study compare to other magnetic latitude ranges, and how ULF dTEC driven from above by ULF waves can be distinguished from driving from below. The publicly available

database (Hartinger, 2024b) and survey plots (Hartinger, 2024a) generated in this study could be used to support future investigations in these areas.

Data Availability Statement

The THEMIS-FAIR-CMO conjunction event database and corresponding survey plots are both publicly available on Zenodo (Hartinger, 2024a, 2024b). The original, unprocessed measurements were obtained from USGS, THEMIS repository (CDAWeb), and NASA CDDIS as described in Section 2.1. Additionally, publicly available THEMIS All Sky Imager measurements used in Movie S1 were obtained from the THEMIS database (https://themis.ssl.berkeley.edu/index.shtml). The majority of analysis and visualization was completed with the help of free, open-source software tools such as numpy (Harris et al., 2020), scipy (Virtanen et al., 2020), matplotlib (Hunter, 2007), IPython (Perez & Granger, 2007), pandas (McKinney, 2010), and others (e.g., Millman & Aivazis, 2011). Finally, the simulation output and software used to generate Figure 7 are publicly available on Zenodo (Hartinger & Ozturk, 2024).

Acknowledgments
MDH was supported by NASA awards 80NSSC21K1683, 80NSSC21K1677, and NSF awards AGS-2307204 and AGS-2027210. XS was supported by NASA awards 80NSSC21K1683, 80NSSC21K1677, and NSF awards AGS-1935110 and AGS-2307205. DO and OV were supported by NASA 80NSSC21K1683. YS was supported by NASA 80NSSC23K0413. A portion of this research was carried out at the Jet Propulsion Laboratory, California Institute of Technology, under a contract with NASA. We acknowledge NASA Contract NAS5-02099 and V. Angelopoulos for use of data from the THEMIS Mission. Specifically: C. W. Carlson and J. P. McFadden for use of ESA data; K. H. Glassmeier, U. Auster, and W. Baumjohann for the use of FGM data provided under the lead of the Technical University of Braunschweig and with financial support through the German Ministry for Economy and Technology and the German Center for Aviation and Space (DLR) under Contract 50 OC 0302. We thank the NASA Space Science Data facility for the use of solar wind data and geomagnetic activity indices. We thank the USGS Geomagnetism Program for use of the CMO ground magnetometer measurements. We thank NASA CDDIS for use of the FAIR receiver measurements.

References

Alfonsi, L., Bergeot, N., Cilliers, P. J., De Franceschi, G., Baddeley, L., Correia, E., et al. (2022). Review of environmental monitoring by means of radio waves in the polar regions: From atmosphere to geospace. *Surveys in Geophysics*, *43*(6), 1609–1698. https://doi.org/10.1007/s10712-022-09734-z

Allan, W., Manuel, J. R., & Poulter, E. M. (1991). Magnetospheric cavity modes: Some nonlinear effects. *Journal of Geophysical Research*, *96*(A7), 11461–11473. https://doi.org/10.1029/91JA00657

Angelopoulos, V. (2008). The THEMIS mission. *Space Science Reviews*, *141*(1–4), 5–34. https://doi.org/10.1007/s11214-008-9336-1

Angelopoulos, V., Cruce, P., Drozdov, A., Grimes, E. W., Hatzigeorgiu, N., King, D. A., et al. (2019). The space physics environment data analysis system (SPEDAS). *Space Science Reviews*, *215*(1), 9. https://doi.org/10.1007/s11214-018-0576-4

Archer, M. O., Hartinger, M. D., Walsh, B. M., Plaschke, F., & Angelopoulos, V. (2015). Frequency variability of standing Alfvén waves excited by fast mode resonances in the outer magnetosphere. *Geophysical Research Letters*, *42*(23), 10150–10159. https://doi.org/10.1002/2015GL066683

Auster, H. U., Glassmeier, K. H., Magnes, W., Aydogar, O., Baumjohann, W., Constantinescu, D., et al. (2008). The THEMIS fluxgate magnetometer. *Space Science Reviews*, *141*(1–4), 235–264. https://doi.org/10.1007/s11214-008-9365-9

Azeem, I., Crowley, G., Forsythe, V. V., Reynolds, A. S., Stromberg, E. M., Wilson, G. R., & Kohler, C. A. (2020). A new frontier in ionospheric observations: GPS total electron content measurements from ocean buoys. *Space Weather*, *18*(11), e2020SW002571. https://doi.org/10.1029/2020SW002571

Belakhovsky, V., Pilipenko, V., Murr, D., Fedorov, E., & Kozlovsky, A. (2016). Modulation of the ionosphere by Pc5 waves observed simultaneously by GPS/TEC and EISCAT. *Earth Planets and Space*, *68*(1), 102. https://doi.org/10.1186/s40623-016-0480-7

Béniguel, Y., Adam, J. P., Jakowski, N., Noack, T., Wilken, V., Valette, J. J., et al. (2009). Analysis of scintillation recorded during the PRIS measurement campaign. *Radio Science*, *44*(4), RS0A30. https://doi.org/10.1029/2008RS004090

Bentley, S. N., Stout, J. R., Bloch, T. E., & Watt, C. E. J. (2020). Random forest model of ultralow-frequency magnetospheric wave power. *Earth and Space Science*, *7*(10), e01274. https://doi.org/10.1029/2020EA001274

Bertiger, W., Bar-Sever, Y., Dorsey, A., Haines, B., Harvey, N., Hemberger, D., et al. (2020). GipsyX/RTGx, a new tool set for space geodetic operations and research. *Advances in Space Research*, *66*(3), 469–489. https://doi.org/10.1016/j.asr.2020.04.015

Borries, C., Ferreira, A. A., Nykiel, G., & Borges, R. A. (2023). A new index for statistical analyses and prediction of travelling ionospheric disturbances. *Journal of Atmospheric and Solar-Terrestrial Physics*, *247*, 106069. https://doi.org/10.1016/j.jastp.2023.106069

Buchert, S. C., Fujii, R., & Glassmeier, K. H. (1999). Ionospheric conductivity modulation in ULF pulsations. *Journal of Geophysical Research*, *104*(A5), 10119–10134. https://doi.org/10.1029/1998JA900180

Cao, M., McPherron, R. L., & Russell, C. T. (1994). Statistical study of ULF wave occurrence in the dayside magnetosphere. *Journal of Geophysical Research*, *99*(A5), 8731–8754. https://doi.org/10.1029/93JA02905

Clauer, C. R., & Ridley, A. J. (1995). Ionospheric observations of magnetospheric low-latitude boundary layer waves on August 4, 1991. *Journal of Geophysical Research*, *100*(A11), 21873–21884. https://doi.org/10.1029/95JA00678

Davies, K., & Hartmann, G. K. (1976). Short-period fluctuations in total columnar electron content. *Journal of Geophysical Research*, *81*(19), 3431–3434. https://doi.org/10.1029/JA081i019p03431

Dinsmore, R., Mathews, J. D., Coster, A., Robinson, R. M., Sarkhel, S., Erickson, P. J., & Urbina, J. (2021). Multi-instrument observations of SCIPS: 1. ISR and GPS TEC results. *Journal of Atmospheric and Solar-Terrestrial Physics*, *213*, 105515. https://doi.org/10.1016/j.jastp.2020.105515

Engebretson, M., Glassmeier, K.-H., Stellmacher, M., Hughes, W. J., & Lühr, H. (1998). The dependence of high-latitude Pc5 wave power on solar wind velocity and on the phase of high-speed solar wind streams. *Journal of Geophysical Research*, *103*(A11), 26271–26384. https://doi.org/10.1029/97JA03143

Grimes, E. W., Harter, B., Hatzigeorgiu, N., Drozdov, A., Lewis, J. W., Angelopoulos, V., et al. (2022). The space physics environment data analysis system in Python. *Frontiers in Astronomy and Space Sciences*, *9*, 1020815. https://doi.org/10.3389/fspas.2022.1020815

Hajj, G. A., & Romans, L. J. (1998). Ionospheric electron density profiles obtained with the Global Positioning System: Results from the GPS/MET experiment. *Radio Science*, *33*(1), 175–190. https://doi.org/10.1029/97RS03183

Harris, C. R., Millman, K. J., van der Walt, S. J., Gommers, R., Virtanen, P., Cournapeau, D., et al. (2020). Array programming with NumPy. *Nature*, *585*(7825), 357–362. https://doi.org/10.1038/s41586-020-2649-2

Hartinger, M. (2024a). Total electron content and magnetic field time series survey plots during THEMIS/CMO/FAIR magnetic conjunctions [Dataset]. *Zenodo*. https://doi.org/10.5281/zenodo.13770417

Hartinger, M. (2024b). ULF wave events during THEMIS-CMO-FAIR magnetic conjunctions [Dataset]. *Zenodo*. https://doi.org/10.5281/zenodo.11536584

Hartinger, M., & Ozturk, D. (2024). Gitm simulation results for figure 7 in manuscript, "statistical analysis of ultra low frequency total electron content disturbances: Relationship to magnetospheric wave" [Dataset]. *Zenodo*. https://doi.org/10.5281/zenodo.14538342

Hartinger, M. D., Angelopoulos, V., Moldwin, M. B., Takahashi, K., & Clausen, L. B. N. (2013). Statistical study of global modes outside the plasmasphere. *Journal of Geophysical Research: Space Physics*, *118*(2), 804–822. https://doi.org/10.1002/jgra.50140

Hartinger, M. D., Moldwin, M. B., Zou, S., Bonnell, J. W., & Angelopoulos, V. (2015). ULF wave electromagnetic energy flux into the ionosphere: Joule heating implications. *Journal of Geophysical Research: Space Physics*, *120*(1), 494–510. https://doi.org/10.1002/2014JA020129

Hartinger, M. D., Takahashi, K., Drozdov, A. Y., Shi, X., Usanova, M. E., & Kress, B. (2022). ULF wave modeling, effects, and applications: Accomplishments, recent advances, and future. *Frontiers in Astronomy and Space Sciences*, *9*, 867394. https://doi.org/10.3389/fspas.2022.867394

Heki, K. (2021). Ionospheric disturbances related to earthquakes. In C. Huang & G. Lu (Eds.), *Ionosphere dynamics and applications* (Vol. 3, pp. 511–526). https://doi.org/10.1002/9781119815617.ch21

Huang, C. Y., Helmboldt, J. F., Park, J., Pedersen, T. R., & Willemann, R. (2019). Ionospheric detection of explosive events. *Reviews of Geophysics*, *57*(1), 78–105. https://doi.org/10.1029/2017RG000594

Hughes, W. J. (1974). The effect of the atmosphere and ionosphere on long period magnetospheric micropulsations. *Planetary and Space Science*, *22*(8), 1157–1172. https://doi.org/10.1016/0032-0633(74)90001-4

Hughes, W. J., & Southwood, D. J. (1976). The screening of micropulsation signals by the atmosphere and ionosphere. *Journal of Geophysical Research*, *81*(19), 3234–3240. https://doi.org/10.1029/JA081i019p03234

Hunter, J. D. (2007). Matplotlib: A 2D graphics environment. *Computing in Science & Engineering*, *9*(3), 90–95. https://doi.org/10.1109/MCSE.2007.55

Jacobs, J. A., Kato, Y., Matsushita, S., & Troitskaya, V. A. (1964). Classification of geomagnetic micropulsations. *Journal of Geophysical Research*, *69*(1), 180–181. https://doi.org/10.1029/JZ069i001p00180

Jayachandran, P. T., Watson, C., Rae, I. J., MacDougall, J. W., Danskin, D. W., Chadwick, R., et al. (2011). High-latitude GPS TEC changes associated with a sudden magnetospheric compression. *Geophysical Research Letters*, *38*(23), L23104. https://doi.org/10.1029/2011GL050041

Juusola, L., Vanhamäki, H., Viljanen, A., & Smirnov, M. (2020). Induced currents due to 3D ground conductivity play a major role in the interpretation of geomagnetic variations. *Annales Geophysicae*, *38*(5), 983–998. https://doi.org/10.5194/angeo-38-983-2020

Kim, H., Clauer, C. R., Deshpande, K., Lessard, M. R., Weatherwax, A. T., Bust, G. S., et al. (2014). Ionospheric irregularities during a substorm event: Observations of ULF pulsations and GPS scintillations. *Journal of Atmospheric and Solar-Terrestrial Physics*, *114*, 1–8. https://doi.org/10.1016/j.jastp.2014.03.006

Kivelson, M. G., & Southwood, D. J. (1988). Hydromagnetic waves and the ionosphere. *Geophysical Research Letters*, *15*(11), 1271–1274. https://doi.org/10.1029/GL015i011p01271

Komjathy, A., Sparks, L., Wilson, B. D., & Mannucci, A. J. (2005). Automated daily processing of more than 1000 ground-based GPS receivers for studying intense ionospheric storms. *Radio Science*, *40*(6), RS6006. https://doi.org/10.1029/2005RS003279

Komjathy, A., Yang, Y.-M., Meng, X., Verkhoglyadova, O., Mannucci, A. J., & Langley, R. B. (2016). Review and perspectives: Understanding natural-hazards-generated ionospheric perturbations using GPS measurements and coupled modeling. *Radio Science*, *51*(7), 951–961. https://doi.org/10.1002/2015RS005910

Kozyreva, O. V., Pilipenko, V. A., Bland, E. C., Baddeley, L. J., & Zakharov, V. I. (2020). Periodic modulation of the upper ionosphere by ULF waves as observed simultaneously by SuperDARN radars and GPS/TEC technique. *Journal of Geophysical Research: Space Physics*, *125*(7), e28032. https://doi.org/10.1029/2020JA028032

Lanzerotti, L. J., Wolfe, A., Trivedi, N., Maclennan, C. G., & Medford, L. V. (1990). Magnetic impulse events at high latitudes: Magnetopause and boundary layer plasma processes. *Journal of Geophysical Research*, *95*(A1), 97–107. https://doi.org/10.1029/JA095iA01p00097

Lotko, W., & Zhang, B. (2018). Alfvénic heating in the cusp ionosphere-thermosphere. *Journal of Geophysical Research: Space Physics*, *123*(12), 10368–10383. https://doi.org/10.1029/2018JA025990

Love, J. J., & Finn, C. A. (2011). The USGS geomagnetism program and its role in space weather monitoring. *Space Weather*, *9*(7), 07001. https://doi.org/10.1029/2011SW000684

Lysak, R. L. (1990). Electrodynamic coupling of the magnetosphere and ionosphere. *Space Science Reviews*, *52*(1–2), 33–87. https://doi.org/10.1007/BF00704239

Lysak, R. L., & Lee, D.-H. (1992). Response of the dipole magnetosphere to pressure pulses. *Geophysical Research Letters*, *19*(9), 937–940. https://doi.org/10.1029/92GL00625

Mannucci, A. J., Wilson, B. D., Yuan, D. N., Ho, C. H., Lindqwister, U. J., & Runge, T. F. (1998). A global mapping technique for GPS-derived ionospheric total electron content measurements. *Radio Science*, *33*(3), 565–582. https://doi.org/10.1029/97RS02707

Martire, L., Runge, T., Meng, X. E. A., Krishnamoorthy, S., Vergados, P., Mannucci, A. J., et al. (2024). The JPL-GIM algorithm and products: Multi-GNSS high-rate global mapping of total electron content. *Journal of Geodesy*, *98*(5), 44. https://doi.org/10.1007/s00190-024-01860-3

Mathie, R. A., & Mann, I. R. (2001). On the solar wind control of Pc5 ULF pulsation power at mid-latitudes: Implications for MeV electron acceleration in the outer radiation belt. *Journal of Geophysical Research*, *106*(A12), 29783–29796. https://doi.org/10.1029/2001JA000002

McFadden, J. P., Carlson, C. W., Larson, D., Ludlam, M., Abiad, R., Elliott, B., et al. (2008). The THEMIS ESA plasma instrument and in-flight calibration. *Space Science Reviews*, *141*(1–4), 277–302. https://doi.org/10.1007/s11214-008-9440-2

McKinney, W. (2010). Data structures for statistical computing in Python. In S. van der Walt & J. Millman (Eds.), *Proceedings of the 9th Python in Science Conference* (pp. 56–61). https://doi.org/10.25080/Majora-92bf1922-012

Meng, X., Mannucci, A. J., Verkhoglyadova, O. P., & Tsurutani, B. T. (2016). On forecasting ionospheric total electron content responses to high-speed solar wind streams. *Journal of Space Weather and Space Climate*, *6*, A19. https://doi.org/10.1051/swsc/2016014

Meng, X., Ozturk, D. S., Verkhoglyadova, O. P., Varney, R. H., Reimer, A. S., Semeter, J. L., et al. (2022). Energy deposition by mesoscale high-latitude electric fields into the thermosphere during the 26 October 2019 geomagnetic storm. *Journal of Geophysical Research: Space Physics*, *127*(12), e2022JA030716. https://doi.org/10.1029/2022JA030716

Meng, X., Vergados, P., Komjathy, A., & Verkhoglyadova, O. (2019). Upper atmospheric responses to surface disturbances: An observational perspective. *Radio Science*, *54*(11), 1076–1098. https://doi.org/10.1029/2019RS006858

Meng, X., Verkhoglyadova, O. P., Komjathy, A., Savastano, G., & Mannucci, A. J. (2018). Physics-based modeling of earthquake-induced ionospheric disturbances. *Journal of Geophysical Research: Space Physics*, *123*(9), 8021–8038. https://doi.org/10.1029/2018JA025253

Millman, K. J., & Aivazis, M. (2011). Python for scientists and engineers. *Computing in Science & Engineering*, *13*(2), 9–12. https://doi.org/10.1109/MCSE.2011.36

Murphy, K. R., Mann, I. R., Rae, I. J., Sibeck, D. G., & Watt, C. E. J. (2016). Accurately characterizing the importance of wave-particle interactions in radiation belt dynamics: The pitfalls of statistical wave representations. *Journal of Geophysical Research: Space Physics*, *121*(8), 7895–7899. https://doi.org/10.1002/2016JA022618

Okuzawa, T., & Davies, K. (1981). Pulsations in total columnar electron content. *Journal of Geophysical Research*, *86*(A3), 1355–1364. https://doi.org/10.1029/JA086iA03p01355

Ozeke, L. G., Mann, I. R., Olifer, L., Dufresne, K. Y., Morley, S. K., Claudepierre, S. G., et al. (2020). Rapid outer radiation belt flux dropouts and fast acceleration during the March 2015 and 2013 storms: The role of ultra-low frequency wave transport from a dynamic outer boundary. *Journal of Geophysical Research: Space Physics*, *125*(2), e27179. https://doi.org/10.1029/2019JA027179

Ozeke, L. G., Mann, I. R., & Rae, I. J. (2009). Mapping guided Alfvén wave magnetic field amplitudes observed on the ground to equatorial electric field amplitudes in space. *Journal of Geophysical Research*, *114*(A1), A01214. https://doi.org/10.1029/2008JA013041

Perez, F., & Granger, B. E. (2007). Ipython: A system for interactive scientific computing. *Computing in Science & Engineering*, *9*(3), 21–29. https://doi.org/10.1109/MCSE.2007.53

Pilipenko, V., Belakhovsky, V., Kozlovsky, A., Fedorov, E., & Kauristie, K. (2014). ULF wave modulation of the ionospheric parameters: Radar and magnetometer observations. *Journal of Atmospheric and Solar-Terrestrial Physics*, *108*, 68–76. https://doi.org/10.1016/j.jastp.2013.12.015

Pilipenko, V., Belakhovsky, V., Murr, D., Fedorov, E., & Engebretson, M. (2014). Modulation of total electron content by ULF Pc5 waves. *Journal of Geophysical Research: Space Physics*, *119*(6), 4358–4369. https://doi.org/10.1002/2013JA019594

Pilipenko, V., Bravo, M., Romanova, N. V., Kozyreva, O. V., Samsonov, S. N., & Sakharov, Y. A. (2018). Geomagnetic and ionospheric responses to the interplanetary shock wave of March 17, 2015. *Izvestiya - Physics of the Solid Earth*, *54*(5), 721–740. https://doi.org/10.1134/S1069351318050129

Poole, A. W. V., & Sutcliffe, P. R. (1987). Mechanisms for observed total electron content pulsations at midlatitudes. *Journal of Atmospheric and Terrestrial Physics*, *49*(3), 231–236. https://doi.org/10.1016/0021-9169(87)90058-4

Pradipta, R., Valladares, C. E., Carter, B. A., & Doherty, P. H. (2016). Interhemispheric propagation and interactions of auroral traveling ionospheric disturbances near the equator. *Journal of Geophysical Research: Space Physics*, *121*(3), 2462–2474. https://doi.org/10.1002/2015JA022043

Pradipta, R., Valladares, C. E., & Doherty, P. H. (2014). GPS observation of continent-size traveling TEC pulsations at the start of geomagnetic storms. *Journal of Geophysical Research: Space Physics*, *119*(8), 6913–6924. https://doi.org/10.1002/2014JA020177

Pulkkinen, A., Bernabeu, E., Thomson, A., Viljanen, A., Pirjola, R., Boteler, D., et al. (2017). Geomagnetically induced currents: Science, engineering, and applications readiness. *Space Weather*, *15*(7), 828–856. https://doi.org/10.1002/2016SW001501

Pulkkinen, A., & Engels, M. (2005). The role of 3-D geomagnetic induction in the determination of the ionospheric currents from the ground geomagnetic data. *Annales Geophysicae*, *23*(3), 909–917. https://doi.org/10.5194/angeo-23-909-2005

Rideout, W., & Coster, A. (2006). Automated GPS processing for global total electron content data. *GPS Solutions*, *10*(3), 219–228. https://doi.org/10.1007/s10291-006-0029-5

Sciffer, M. D., & Waters, C. L. (2011). Relationship between ULF wave mode mix, equatorial electric fields, and ground magnetometer data. *Journal of Geophysical Research*, *116*(A6), A06202. https://doi.org/10.1029/2010JA016307

Shen, Y., Verkhoglyadova, O. P., Artemyev, A., Hartinger, M. D., Angelopoulos, V., Shi, X., & Zou, Y. (2024). Magnetospheric control of ionospheric TEC perturbations via whistler-mode and ULF waves. *AGU Advances*, *5*(6). https://doi.org/10.1029/2024AV001302

Shi, X., Baker, J. B. H., Ruohoniemi, J. M., Hartinger, M. D., Murphy, K. R., Rodriguez, J. V., et al. (2018). Long-lasting poloidal ULF waves observed by multiple satellites and high-latitude SuperDARN radars. *Journal of Geophysical Research: Space Physics*, *123*(10), 8422–8438. https://doi.org/10.1029/2018JA026003

Shi, X., Ruohoniemi, J. M., Baker, J. B. H., Lin, D., Bland, E. C., Hartinger, M. D., & Scales, W. A. (2018). Survey of ionospheric Pc3-5 ULF wave signatures in SuperDARN high time resolution data. *Journal of Geophysical Research: Space Physics*, *123*(5), 4215–4231. https://doi.org/10.1029/2017JA025033

Skone, S. (2009). Using GPS TEC measurements to detect geomagnetic Pc 3 pulsations. *Radio Science*, *44*(19), RS0A27. https://doi.org/10.1029/2008RS004106

Smith, A. R., Ozturk, D. S., Delamere, P., Lu, G., & Kim, H. (2023). Investigating the interhemispheric asymmetry in Joule heating during the 2013 St. Patrick's Day geomagnetic storm. *Space Weather*, *21*(9), e2023SW003523. https://doi.org/10.1029/2023SW003523

Southwood, D. J., & Hughes, W. J. (1983). Theory of hydromagnetic waves in the magnetosphere. *Space Science Reviews*, *35*(4), 301–366. https://doi.org/10.1007/BF00169231

Surkov, V. V., Pilipenko, V. A., & Shiokawa, K. (2023). Geomagnetic effect of the atmospheric acoustic resonance excited by earthquakes and volcano eruptions. *Journal of Geophysical Research: Space Physics*, *128*(10), e2023JA031872. https://doi.org/10.1029/2023JA031872

Takahashi, K., & Anderson, B. J. (1992). Distribution of ULF energy (f<=80 mHz) in the inner magnetosphere: A statistical analysis of AMPTE CCE magnetic field data. *Journal of Geophysical Research*, *97*(A7), 10751–10773. https://doi.org/10.1029/92JA00328

Takahashi, K., & Ukhorskiy, A. Y. (2007). Solar wind control of Pc5 pulsation power at geosynchronous orbit. *Journal of Geophysical Research*, *112*(A11), A11205. https://doi.org/10.1029/2007JA012483

Takahashi, K., Yumoto, K., Claudepierre, S. G., Sanchez, E. R., Troshichev, O. A., & Janzhura, A. S. (2012). Dependence of the amplitude of Pc5-band magnetic field variations on the solar wind and solar activity. *Journal of Geophysical Research*, *117*(A4), A04207. https://doi.org/10.1029/2011JA017120

Themens, D. R., & Jayachandran, P. T. (2016). Solar activity variability in the IRI at high latitudes: Comparisons with GPS total electron content. *Journal of Geophysical Research: Space Physics*, *121*(4), 3793–3807. https://doi.org/10.1002/2016JA022664

Tsunoda, R. T. (1988). High-latitude F-region irregularities: A review and synthesis. *Reviews of Geophysics*, *26*(4), 719–760. https://doi.org/10.1029/RG026i004p00719

Tsyganenko, N. A. (1989). A magnetospheric magnetic field model with a warped tail current sheet. *Planetary and Space Science*, *37*(1), 5–20. https://doi.org/10.1016/0032-0633(89)90066-4

Vadas, S. L. (2007). Horizontal and vertical propagation and dissipation of gravity waves in the thermosphere from lower atmospheric and thermospheric sources. *Journal of Geophysical Research*, *112*(A6), A06305. https://doi.org/10.1029/2006JA011845

Verkhoglyadova, O. P., Meng, X., Mannucci, A. J., & McGranaghan, R. M. (2018). Semianalytical estimation of energy deposition in the ionosphere by monochromatic Alfvén waves. *Journal of Geophysical Research: Space Physics*, *123*(6), 5210–5222. https://doi.org/10.1029/2017JA025097

Virtanen, P., Gommers, R., Oliphant, T. E., Haberland, M., Reddy, T., Cournapeau, D., et al. (2020). SciPy 1.0: Fundamental algorithms for scientific computing in Python. *Nature Methods*, *17*(3), 261–272. https://doi.org/10.1038/s41592-019-0686-2

Vorob'Ev, V., & Krasil'nikova, T. (1994). Estimation of accuracy of the atmosphere refractive index recovery from Doppler shift measurements at frequencies used in the NAVSTAR system. *Isvestiya Russian Academy of Sciences, Physics of the Atmosphere and Ocean, English Translation*, *29*(5), 602–609.

Walker, A. D. M., Greenwald, R. A., Stuart, W. F., & Green, C. A. (1979). Stare auroral radar observations of Pc 5 geomagnetic pulsations. *Journal of Geophysical Research*, *84*(A7), 3373–3388. https://doi.org/10.1029/JA084iA07p03373

Wang, B., Nishimura, Y., Hartinger, M., Sivadas, N., Lyons, L. L., Varney, R. H., & Angelopoulos, V. (2020). Ionospheric modulation by storm time Pc5 ULF pulsations and the structure detected by PFISR-THEMIS conjunction. *Geophysical Research Letters*, *47*(16), e89060. https://doi.org/10.1029/2020GL089060

Waters, C. L., & Cox, S. P. (2009). ULF wave effects on high frequency signal propagation through the ionosphere. *Annales Geophysicae*, *27*(7), 2779–2788. https://doi.org/10.5194/angeo-27-2779-2009

Watson, C., Jayachandran, P. T., & MacDougall, J. W. (2016a). Characteristics of GPS TEC variations in the polar cap ionosphere. *Journal of Geophysical Research: Space Physics*, *121*(5), 4748–4768. https://doi.org/10.1002/2015JA022275

Watson, C., Jayachandran, P. T., & MacDougall, J. W. (2016b). GPS TEC variations in the polar cap ionosphere: Solar wind and IMF dependence. *Journal of Geophysical Research: Space Physics*, *121*(9), 9030–9050. https://doi.org/10.1002/2016JA022937

Watson, C., Jayachandran, P. T., Singer, H. J., Redmon, R. J., & Danskin, D. (2015). Large-amplitude GPS TEC variations associated with Pc5-6 magnetic field variations observed on the ground and at geosynchronous orbit. *Journal of Geophysical Research: Space Physics*, *120*(9), 7798–7821. https://doi.org/10.1002/2015JA021517

Watson, C., Jayachandran, P. T., Singer, H. J., Redmon, R. J., & Danskin, D. (2016). GPS TEC response to Pc4 "giant pulsations". *Journal of Geophysical Research: Space Physics*, *121*(2), 1722–1735. https://doi.org/10.1002/2015JA022253

Watson, C., Jayachandran, P. T., Spanswick, E., Donovan, E. F., & Danskin, D. W. (2011). GPS TEC technique for observation of the evolution of substorm particle precipitation. *Journal of Geophysical Research*, *116*(A10), A00I90. https://doi.org/10.1029/2010JA015732

Welling, D. (2019). Magnetohydrodynamic models of b and their use in gic estimates. In *Geomagnetically induced currents from the sun to the power grid* (pp. 43–65). American Geophysical Union (AGU). https://doi.org/10.1002/9781119434412.ch3

Wild, J. A., Yeoman, T. K., & Waters, C. L. (2005). Revised time-of-flight calculations for high-latitude geomagnetic pulsations using a realistic magnetospheric magnetic field model. *Journal of Geophysical Research*, *110*(A11), A11206. https://doi.org/10.1029/2004JA010964

Yizengaw, E., Zesta, E., Biouele, C. M., Moldwin, M. B., Boudouridis, A., Damtie, B., et al. (2013). Observations of ULF wave related equatorial electrojet and density fluctuations. *Journal of Atmospheric and Solar-Terrestrial Physics*, *103*, 157–168. https://doi.org/10.1016/j.jastp.2013.03.015

Yizengaw, E., Zesta, E., Moldwin, M. B., Magoun, M., Tripathi, N. K., Surussavadee, C., & Bamba, Z. (2018). ULF wave-associated density irregularities and scintillation at the equator. *Geophysical Research Letters*, *45*(11), 5290–5298. https://doi.org/10.1029/2018GL078163

Zhai, C., Shi, X., Wang, W., Hartinger, M. D., Yao, Y., Peng, W., et al. (2021). Characterization of high-m ULF wave signatures in GPS TEC data. *Geophysical Research Letters*, *48*(14), e94282. https://doi.org/10.1029/2021GL094282